Supporting Information

Fluoroalkyl-Functionalized Cyclic Ethers as Solvent for High-Voltage Batteries

Ke-Hsin Wang,[1] Ritesh Kumar,[1] Peiyuan Ma,[1] Jaemin Kim,[2] Bitgaram Kim,[1] and Chibueze V. Amanchukwu[1*]

[1]Pritzker School of Molecular Engineering, University of Chicago, IL 60637 USA

[2]Department of Chemistry, University of Chicago, IL 60637 USA

*Corresponding author

Email: chibueze@uchicago.edu

Experimental section

Materials. 1,2-dimethoxyethane (DME, 99%, inhibitor-free, Sigma-Aldrich), 3-hydroxyltetrahydrofuran (98%, Ambeed), potassium hydroxide (85%, Fisher Scientific), p-toluenesulfonyl chloride (Ambeed), 2,2-difluoroethan-1-ol (98%, TCI), 2,2,2-rrifluoroethanol (99%, Sigma-Aldrich), 1H,1H-pentafluoropropan-1-ol (98%, Synquest lab), 2,2,3,3,4,4,4-heptafluoro-1-butanol (98%, Sigma-Aldrich), 2,3-dihydrofuran (98%, Fisher Scientific), p-toluenesulfonic acid monohydrate (97%, Combi-blocks), sodium sulfate (anhydrous, Fisher Scientific), magnesium sulfate, (anhydrous, $MgSO_4$, Fisher Scientific), sodium hydride (NaH, 60%, in mineral oil, Sigma-Aldrich), calcium hydride (95%, CaH_2, Oakwood chemicals), dichloromethane (DCM, 99.5%, Fisher Scientific), and diethyl ether (Fisher Scientific, stabilized with BHT) were used as received. α,α,α-trifluorotoluene (99%, Sigma-Aldrich), deuterated acetonitrile (d_3-ACN, 99.8 atom % D, Cambridge Isotope Laboratories), deuterated chloroform ($CDCl_3$, 99.5 atom % D, Cambridge Isotope Laboratories), deuterated dimethyl sulfoxide (DMSO-d_6, 99.9 atom % D, Cambridge Isotope Laboratories), and 1,1,2,2-tetrafluoroethyl 2,2,3,3-tetrafluoropropyl ether (TTE, 99.5% battery grade, Synquest lab) were used after drying with 4A molecular sieves for 3 days.

Synthesis. DFETHF (3-(2,2-difluoroethoxy)oxolane), TFETHF (3-(2,2,2-trifluoroethoxy)oxolane), PFPTHF (3-(2,2,3,3-pentafluoropropoxy)oxolane), and SFBTHF (3-(2,2,3,3,4,4,4-heptafluorobutoxy)oxolane) are synthesized via the same way. To synthesize DFETHF , 3-hydroxyltetrahydrofuran was first tosylated using the same method as previously reported.[1] Specifically, 25g of 3-hydroxyltetrahydrofuran was mixed with 59 g of p-TsCl (1.1 equiv) in DCM (dichloromethane, 200 mL). After the homogeneous solution was cooled to 0°C for 15 minutes, 32 g of KOH powder was added portionwise. The suspension was slowly heated up to room temperature overnight to ensure complete reaction. To purify the target compound, the solution was diluted with 100 mL DCM and quenched with water first. After being extracted with brine (saturated NaCl in H_2O) 3 times, the organic phase was collected and dried with Na_2SO_4. DCM was removed by rotary evaporator and colorless crystals were obtained as tosylated THF. Next, the tosylated THF (28 g, 1.2 equiv.) and the fluoro-alcohol, 2,2-difluoroethan-1-ol (14.3 g, 1.0 equiv.), were dissolved in 30 mL NMP (N-methyl pyrrolidone) to

form a homogeneous solution. After the solution was cooled to 0°C using an ice bath, 45 wt% KOH (2.4 equiv.) aqueous was added dropwise to the reaction flask. The solution was slowly warmed up to 40°C and stirred overnight. Then, it was stirred at 70°C for 3 hours for complete reaction. To purify the compound, the solution was filtered and the solid was washed with diethyl ether twice. The filtrate was collected and extracted with water once and brine (saturated NaCl in H_2O) twice. After being dried with Na_2SO_4, diethyl ether was removed by rotary evaporator. Excess amount of NaH was added to remove trace water in the mixture before distillation. Two successive distillations afforded the final product, which was collected at 76°C under 60 mbar (yield: 12.1%). TFETHF, PFPTHF, and SFBTHF were synthesized via the same route with corresponding fluoro-alcohol (2,2,2-trifluoroethanol for TFETHF, 1H,1H-pentafluoropropan-1-ol for PFPTHF, and 2,2,3,3,4,4,4-heptafluoro-1-butanol for SFBTHF). The yield was 33.6%, 33,4%, and 23.9% for TFETHF, PFPTHF, and SFBTHF respectively.

To synthesize 2DFETHF, 2,3-dihydrofuran (10 g, 1.4 equiv.) and the fluoro-alcohol, 2,2-difluoroethan-1-ol (10 g, 1.0 equiv.), were first dissolved in 100 mL DCM. Catalytic amount of p-toluenesulfonic acid monohydrate (2.3 g, 10 mol %) was added to the solution at room temperature and stirred overnight. To purify the target compound, the transparent yellow mixture was first extracted with diethyl ether 0.1 M KOH, followed by brine extraction twice. After drying the organic phase over $MgSO_4$, DCM (dichloromethane) and diethyl ether in the mixture was removed with rotary evaporator. Then, the mixture was added to CaH_2 and heated up to 40°C for 3 hours. Fractional distillation was performed twice to obtain the final product (yield: 16.8%). 3TFETHF and 3PFPTHF were synthesized via the same route using corresponding fluoro-alcohol (2,2,2-trifluoroethanol for 2TFETHF, 1H,1H-pentafluoropropan-1-ol for 2PFPTHF). The yield was 25.3% for 2TFETHF and 50.8% for 2PFPTHF.

All electrolytes were prepared by adding solvent to weighted LiFSA salt in an argon-filled glovebox (O_2 and H_2O < 1 ppm). All the electrolytes have water content lower than 100 ppm measured by Karl Fisher titration (Mettler Toledo C10S Compact).

Characterization.

NMR Spectroscopy. ^{1}H, ^{13}C, ^{19}F, and ^{7}Li NMR were performed on a Bruker Ascend 9.4 T/400 MHz instrument. Sample preparation was done in an argon-filled glovebox (Vigor, O_2 and H_2O < 1 ppm). Spectra taken for the electrolyte oxidative stability test were obtained by immersing

the separator of cycled cells in 0.5 mL of DMSO-d_6 for 3 minutes. The other spectra were prepared by the capillary setup, where a sealed capillary containing the sample electrolyte was placed in an NMR tube pre-filled with CD_3CN. Pulsed-field gradient NMR (PFG-NMR) was also performed with the capillary setup to measure the diffusivity of ions following the method reported elsewhere.[1]

Raman Spectroscopy. In an argon-filled glovebox, the samples were sealed in a glass chamber containing a set of glass slide (Chemglass life science) and a sheet of silicone isolator (Grace Bio-Laboratories). Raman spectra were taken by a HORIBA LabRAM HR Evolution confocal Raman microscope using a 532 nm ULF laser as the light source.

Viscosity. microVISC viscometer (RheoSense) was used to measure viscosity. Around 200 μL of the sample was injected into the viscometer via syringe. The syringe filled with the sample was taken from the argon-filled glovebox right before each measurement.

Scanning Electron Microscopy (SEM). The samples for observing Li deposition were prepared by cycling Li||Cu cells at 0.5 mA/cm^2 to 1.5 mA h/cm^2 after 5 cleaning precycles from 0 to 1 V at 0.02 mA/cm^2. Afterwards, the cells were opened in an argon-filled glovebox, and the Cu current collector was gently washed with DME (1,2-dimethoxyethane) three times. The Cu foil was then dried under vacuum and sealed under argon before being transferred into the chamber of the Carl Zeiss Merlin field emission scanning electron microscope for measurement. The sample was exposed to air for around 30 seconds before being transferred to the SEM chamber.

X-ray Photoelectron Spectroscopy (XPS). The samples with Li deposition were prepared in the same way as those for SEM measurements. They were transferred to a ThermoFisher Scientific XPS: NEXSA G2 using an air-free sample holder. To obtain the depth profile, an EX06 monatomic Ar ion source was used as the etching source. The cathode samples were cycled in Li||NMC811 cells for 97 cycles at C/3 before de-crimping. Three C/10 precycles were done before the cells were cycled at C/3. The cathodes were washed with DME three times and dried under vacuum before being transferred to the equipment. The samples were not exposed to air at any time.

SEI titration. SEI is formed in Li||Cu coin cells under 5 cycles at 0.5 mA/cm^2. Li is deposited to 1.5 mAh/cm^2 and stripped to 1V for each cell. After cycling, coin cells were de-crimped in an

Argon-filled glovebox, and the Cu foil and separator of each cell were carefully sealed in a separate septum vial. To quantify dead Li, the vial containing SEI on Cu foil was taken out of the glovebox and we added 0.5 mL of 3.5 M $HClO_4$ to the vial. After 3 minutes of reaction, 2 mL of the head space of the septum vial was taken out using an airtight syringe (Hamilton) and injected into a Shimadzu GC-2014 gas chromatograph. H_2 produced by acid titration was detected by thermally conductive detectors. To quantify LiF amount, 1.0 mL H_2O was added to the vial. After 12 hours of reaction, 100 µL of the titrated sample was mixed with 400 µL of standard solution (2 mM 2-difluoroethanol in D_2O), and the LiF amount was quantified by the relative integral of 2-difluoroethanol in ^{19}F NMR spectroscopy. The percentage of capacity loss is calculated as the capacity required to form the species detected by the titration method divided by the total capacity loss measured by the potentiostat.

X-Ray Diffraction. Cycled Li||NMC811 cells were de-crimped in an Argon-filled glovebox and washed with DME three times. After drying under vacuum for 10 minutes, the cathode was sealed with Kapton tape and Kapton board. After the sample was taken out from the glovebox, it was tested in a Rigaku SmartLab X-ray diffractometer, equipped with Cross-Beam-Optics (CBO) and the HyPix-3000 detector. Cu Kα was used as the radiation source in the 2θ range from 10 to 80 degrees with a step of 0.1° and a scan rate of 10° min^{-1}.

Electrochemical tests.

E_{Li} Tests. Lithium potential of each electrolyte was tested in a Li||Pt beaker cell with the addition of 1 mM ferrocene as the reference following the method in previous work.[1]

Battery Tests. All battery tests were performed in CR2032 type coin cells (Xiamen TOB New Energy Technology) following the configuration below: negative case||spring||anode||25µL electrolyte||Celgard 2325 (Celgard LLC., 18 mm in diameter) ||25µL electrolyte||cathode||positive case. For any cell cycled above 4 V versus Li/Li^+, an Al-coated cap was used, and an Al foil (Battery grade, MSE Supplies) was added between the cathode and the positive coin cell case. All coin cells were fabricated in an argon-filled glovebox. Thick Li (500 µm thickness, 12 mm in diameter) was used unless otherwise specified. Electrolyte conductivity was calculated from the resistance measured via electrochemical impedance spectroscopy test and the values were calibrated using 0.2 M fluorinated cyclic ether. Details of the measurement and calibration method are described elsewhere.[1] Li||Al LSV, Li||Al potentiostatic hold test, Li||Cu Aurbach test,

Li||Li coin cell cycling, and 20 μm Li||LFP coin cell cycling were performed following the procedures reported in previous work.[1] Li||NMC811 cells were cycled in a voltage between 3.0-4.4 V at C/3 after 3 formation cycle at C/10. LFP loading ≈ 1.86 mA h/cm^2. NMC loading ≈ 1.66 mA h/cm^2.

Classical molecular dynamics (MD).

Non-polarizable force field MD. All the non-polarizable classical MD calculations were performed using LAMMPS (Large Scale Atomic/Molecular Massively Parallel Simulator[2]) simulation package (version September 2021). To parametrize the solvent molecules, the non-polarizable optimized potential for liquid simulations (all-atom) (OPLS-AA[3]) force fields were employed. All the OPLS-AA force-field parameters were extracted from the LigParGen web server,[4] developed by W. L. Jorgensen *et. al*. The partial charges were obtained by scaling CM1A charges by a factor of 1.14[5] and assigned based on atom types. The force field parameters including partial charges (scaled by 0.8) for Li^+ and FSA^- ions were taken from Lopes *et al.*[6] To create the simulation box, three-dimensional periodic boundary conditions were applied, containing approximately 700 solvent molecules with salt concentration fixed at 1 M. PACKMOL[7] was utilized to create initial configurations, having a volume of 50×50×50 Å^3, generated by randomly placing solvent, Li^+, and FSA^- ions. The initial configurations were optimized using the steepest descent minimization algorithm until total energy and each component of force on every atom converged to 1×10^{-5} and 1×10^{-7} kcal mol^{-1} Å^{-1}, respectively. Following energy minimization, the systems were equilibrated for 0.5 ns in an NPT ensemble using a Nose-Hoover barostat at 1 bar and a Nose-Hoover thermostat at 300 K. Subsequently, all the systems underwent annealing at 500 K in an NVT ensemble for 0.5 ns (to avoid confinement in the initial configuration), followed by another NVT ensemble calculation at 300 K for 0.5 ns using the Nose–Hoover thermostat. The final production runs were performed in the NVT ensemble at 300 K using the same settings for a duration of 30 ns. All MD calculations were performed with a time step of 1 fs. The MD snapshots were saved every 10 ps for electrolytes during the production run.

Polarizable force field MD. The force fields generation, set-up of initial box, and all MD runs were performed using a software 'byteff2', which is openly available at https://github.com/ByteDance-Seed/byteff2. This software uses ByteFF-Pol[8] polarizable force-

fields to parametrize both solvents and salts as well as non-bonding interactions. It then uses GROMACS[9] to randomly pack solvent and salt molecules into boxes of initial volume 50×50×50 $Å^3$ (number of solvent and salt molecules in **Table S4**). And the polarizable classical MD calculations are performed using OpenMM.[10] The initial configurations were optimized using the Limited-memory Bryden-Fletcher-Goldfarb-Shanno (L-BFGS) algorithm until root mean square of all force components reaches a tolerance of 10 kJ mol^{-1} nm^{-1}, respectively. Following energy minimization, the systems were equilibrated for 3 ns in an NPT ensemble using a Monte Carlo barostat at 1 atm and a Langevin thermostat at 298 K. The final production runs were performed in the NVT ensemble at 298 K using the Langevin thermostat for a duration of 30 ns. All MD calculations were performed with a time step of 2 fs. The MD snapshots were saved every 1 ps for electrolytes during the production run.

Analysis of MD trajectories. All trajectories saved during the production runs were used to calculate the radial distribution function (RDF), domain network index (I_d), and transport properties. The RDFs were computed using the MDAnalysis[11] python library (version 2.3.0). The I_d values were calculated using a python code developed in-house. All transport properties, i.e., ionic conductivity, diffusivity of lithium cation and FSA anions, as well as transference number of lithium ions were computed using the code from the byteff2[12] GitHub repository employing Onsager formalism. All the MD snapshot visualizations have been generated using the ChimeraX[13] program.

Comparison between non-polarizable and polarizable force fields. The comparison in ionic conductivity, diffusivity of Li cation and FSA anions, as well as transference number of Li^+ ions calculated using OPLS and ByteFF-Pol force fields are summarized in Figure S6 as bar plots. While there is no consistent trend error in OPLS- and ByteFF-Pol-calculated transport properties (with respect to experimental values) for the four electrolytes, we find that OPLS force field underestimates the properties to significant extent, in general. On the other hand, ByteFF-Pol overestimates these properties only slightly. Therefore, the error in values is much smaller when using the ByteFF-Pol force field (lower mean absolute error (MAE)), except for diffusivity of Li^+ ions, where OPLS is slightly more accurate (Fig. S6(b)). Therefore, we reported the ByteFF-Pol force field-derived transport properties and solvation behavior in the present work.

Density functional theory.

All DFT calculations including binding energies, LUMO energy levels, ESP, and solvent-cation affinity were performed using Gaussian 16[14] (version 16.0.1) program. B3LYP and 6-311**g(d,p) was utilized as the functional and basis sets, respectively. Implicit solvation corrections considering tetrahydrofuran (THF) as the solvent were also included using the polarizable continuum model (PCM) method. ESP map visualization was carried out using ChimeraX[13] program. The solvation clusters consisting of three solvent molecules and one FSA anion bound to a single Li^+ ion, i.e., a contact-ion pair (CIP; this particular cluster found to be most predominant from MD calculations among all types of clusters possible and CIPs are also found to be highly dominant from Raman spectra in Figure S4(b)) were extracted randomly from the polarizable MD production runs and solvation energies ($\Delta E_{solvation}$) were evaluated according to the following expression:

$$\Delta E_{solvation} = E_{solv-Li^+-FSA^-} - 3 \cdot E_{solv} - E_{Li^+} - E_{FSA^-} \quad \text{(S1)}$$

where $E_{solv-Li^+-FSA^-}$, E_{solv}, E_{Li^+}, E_{FSA^-} are DFT-optimized energies of the CIP cluster, single isolated solvent, isolated Li cation, and isolated FSA anion with implicit solvation correction. A more negative solvation energy value denotes higher thermodynamic stability. The optimized CIP clusters extracted from polarizable MD trajectory for the four electrolytes are shown in Figure S6 along with the corresponding solvation energy values. Since solvation energy of the CIP cluster decreases from DFETHF to SFBTHF, we conclude that ion pair formation is thermodynamically more stable in SFBTHF compared to other electrolytes.

Supplementary Note 1: Influence of cation–anion interaction on conductivity

To better understand the decrease in ionic conductivity with increasing fluorination degree, we performed a Walden plot analysis (**Figure S7a**) to evaluate electrolyte non-ideality arising from ion aggregation. In an ideal system with fully dissociated ions, the molar conductivity scales inversely with viscosity, resulting in a linear relationship where the product of ionic conductivity and viscosity remains constant. However, the fluorinated cyclic ether electrolytes studied here deviate from this ideal line, indicating that viscosity alone cannot fully account for the observed decrease in ionic conductivity at higher fluorination degrees.

The deviation from the ideal line in Figure S7a reflects non-ideal behavior associated with incomplete ion dissociation and aggregation. The ionicity quantified by the distance of each data point from the ideal line (**Figure S7b**) shows that ion aggregation is more pronounced in TFETHF, PFPTHF, and SFBTHF than in DFETHF. These results suggest that, in addition to increased viscosity, enhanced ion aggregation also contributes to the reduced ionic conductivity of highly fluorinated cyclic ethers.

Supplementary Note 2: Structural effects on solvation at a constant F/O ratio

We have observed that the electrolyte using F5DEE shows weaker solvation than that of PFETHF while both have the same numbers of oxygen and fluorine atoms. One possible explanation for this difference is that fluorination sites on PFETHF are far from the oxygen atom on the THF ring, which is the molecule's primary coordination site. Compared to F5DEE, which has fluorine atoms adjacent to both oxygen atoms, the electron-withdrawing and steric hindrance effect of fluorine atoms on the oxygen in the ring of PFPTHF could be mild, leading to weaker disruption of Li^+–solvent interactions. The sharp difference in electron density is reflected in the differences in ESP values on the oxygen atoms shown in **Figures S9c** and **Figures S9e**.The effect of electron density could also be observed in 2PFPTHF, an isomer of PFPTHF. The solvent molecules fluorinated at the 2' position were synthesized for comparison. Raman spectra of the corresponding electrolytes at the same salt concentration show a more pronounced blue shift in the region of interest, indicating that Li^+–O interactions are weaker when the fluoroalkyl side chain is positioned closer to the primary solvation site (ESP values on oxygen atoms in **Figure S9f** and S–N–S Raman stretching mode in **Figure S10**).

Supplementary Note 3: Cathode characterization of Li||NMC811 cells to understand failure in 3FTHF under high voltage

To understand the performance of SFBTHF compared to early cell failure (capacity dropping below 80% within 50 cycles) of 3FTHF electrolyte in Li||NMC811 cells, post-mortem X-ray diffraction (XRD) analysis was used and analyzed together with dQ/dV plots of the 47th cycle (**Figure S17**).

The Li||NMC811 cells ending on charge are analyzed electrochemically and de-crimped for XRD analysis. The dQ/dV profiles of the last full cycles (discharging half cycle of the 46th cycle and charging half cycle of the 47th cycle) are shown in **Figure S17a** and **b**. The cathode using SFBTHF electrolyte shows three distinct phase transitions[15] (H1→M, M→H2, and H2→H3 represented by peaks a, b, and c in **Figure S17a**), indicating complete phase evolution during cycling. In contrast, the 3FTHF electrolyte shows only two apparent transitions (peaks α and β in **Figure S17b**) along with significant charge-discharge hysteresis, suggesting increased polarization and incomplete phase transition from H1 to H3.

This electrochemical signature is consistent with the XRD analysis of NMC811 cathodes after 45 cycles, compared with both the pristine cathode and the cathode at early charged states using the SFBTHF electrolyte (**Figure S17c** and **d**). During charging, NMC811 is known to undergo anisotropic lattice changes, where the c-axis initially expands and then contracts.[16] As shown in **Figure S17d**, a notable difference is observed in the (003) peak, which tracks changes along the c-axis. The cathode cycled in SFBTHF exhibits a contracted c-axis relative to the expanded state, approaching or even slightly below that of the pristine structure. In contrast, the cathode cycled in 3FTHF remains in an expanded state relative to the pristine cathode.

These results indicate that the incomplete phase evolution in 3FTHF after charge to 4.4 V is reflected on the expanded c-axis, and it leads to capacity loss of Li||NMC811 cells. In comparison, SFBTHF supports full phase transitions and the expected lattice contraction, correlating with improved cycling stability.

Supplementary Note 4: SEI composition and formation mechanism of electrolytes containing highly fluorinated cyclic ethers

In this work, the SEI composition is characterized at both the surface and bulk levels. Surface analysis by XPS shows that SEI formed in highly fluorinated electrolytes contains higher fractions of LiF and Li_2O (**Figure S20**). Consistently, bulk quantification using a titration method indicates reduced capacity loss from dead Li and increased capacity loss from LiF content with increasing fluorination degree (**Figure S21**). These observations are in good agreement with reported trends for high-CE electrolytes[17, 18], suggesting that heavily fluorinated cyclic ethers (PFPTHF and SFBTHF) show features commonly associated with improved lithium reversibility compared to less fluorinated counterparts (DFETHF and TFETHF), including lower dead Li and more inorganic-rich SEI components.

This behavior may be related to the relatively weak solvation strength of highly fluorinated ethers, which can promote increased anion participation in interfacial reactions. In this context, decomposition of FSA^- may contribute to the formation of Li_2O and LiF species.[18] These inorganic components are generally considered to form protective SEI layers that help limit continuous electrolyte decomposition and reduce dead Li accumulation.[19]

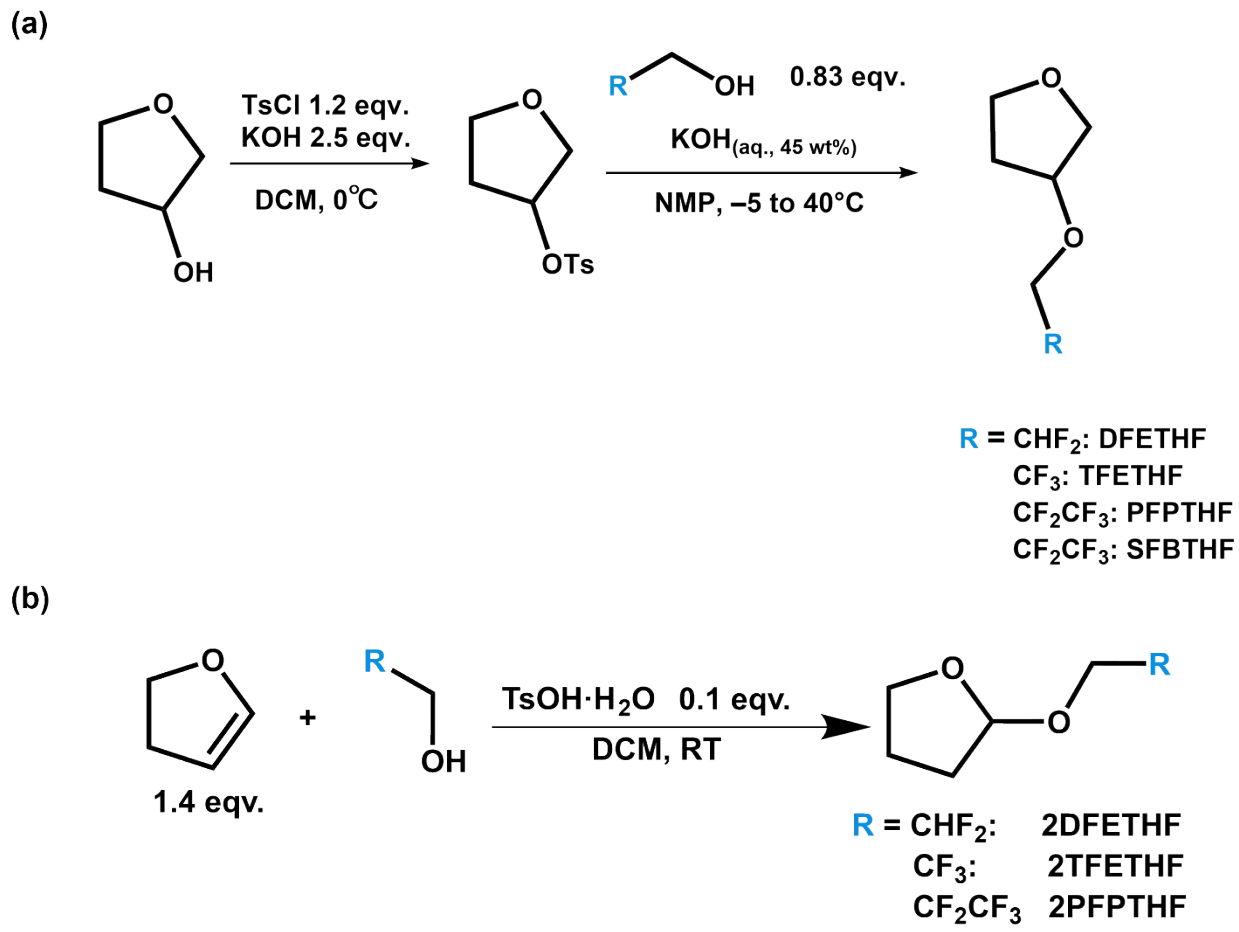

Figure S1 Synthetic route of fluoroalkyl cyclic ethers. (**a**) Cyclic ethers with fluoroalkyl groups on the 3' position of THF ring. (**b**) Cyclic ethers with fluoroalkyl groups on the 2' position of THF ring.

(a1)

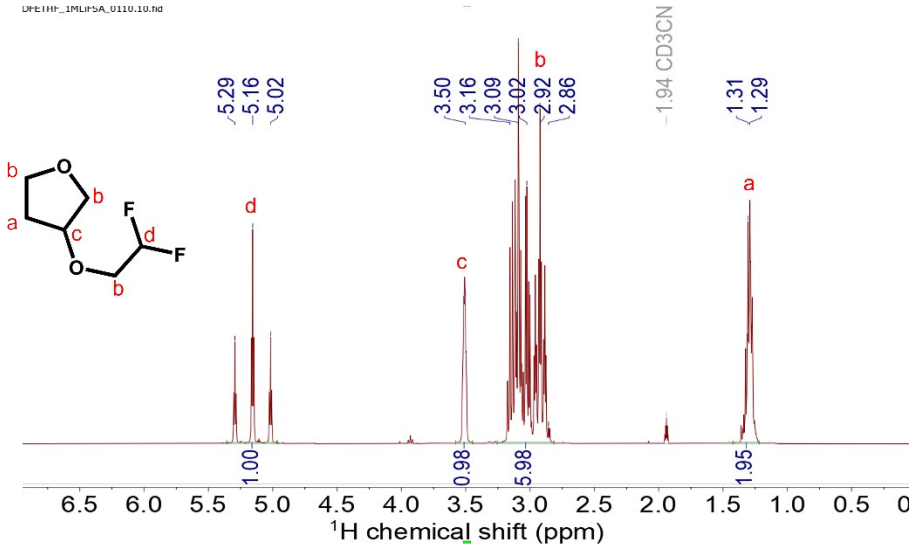
5.29
5.16
5.02
3.50
3.16
3.09
3.02
2.92
2.86
1.94 CD3CN
1.31
1.29
1.00
0.98
5.98
1.95
6.5 6.0 5.5 5.0 4.5 4.0 3.5 3.0 2.5 2.0 1.5 1.0 0.5 0
^{1}H chemical shift (ppm)

(a2)

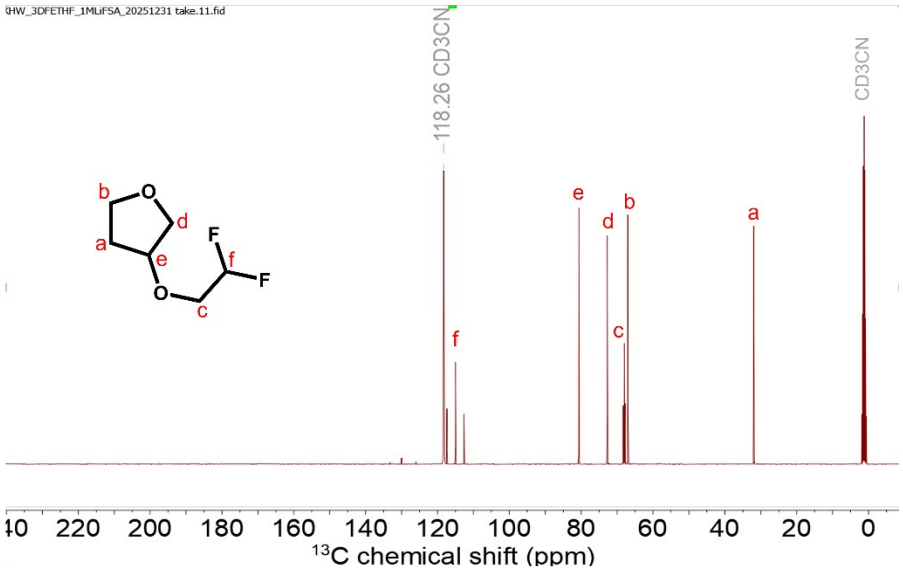
118.26 CD3CN
CD3CN
40 220 200 180 160 140 120 100 80 60 40 20 0
^{13}C chemical shift (ppm)

(a3)

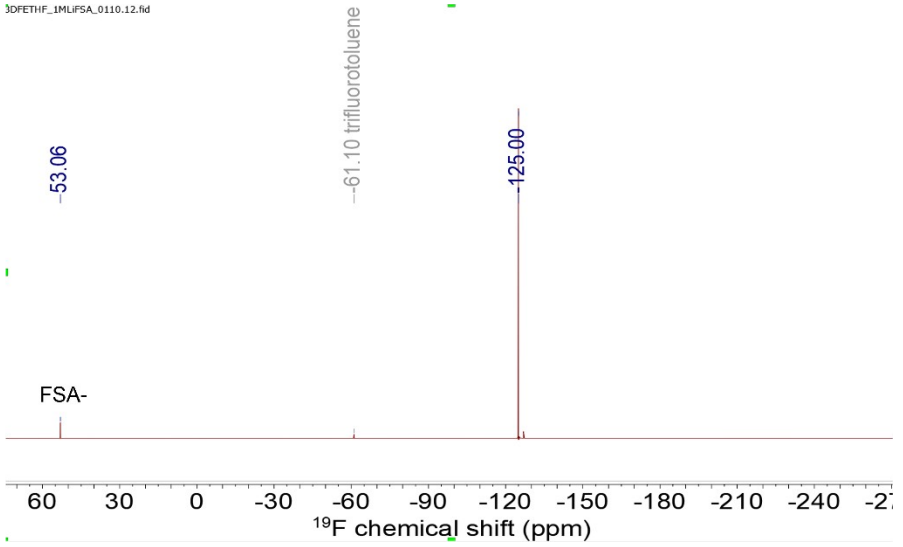
53.06
61.10 trifluorotoluene
125.00
FSA-
60 30 0 -30 -60 -90 -120 -150 -180 -210 -240
^{19}F chemical shift (ppm)

(b1)

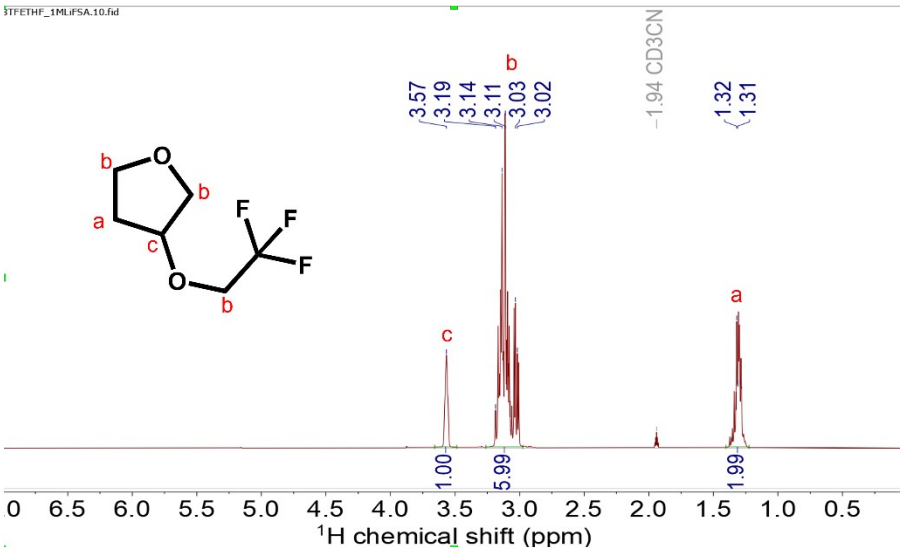
3TFETHF_1MLiFSA.10.fid
3.57
3.19
3.14
3.11
3.03
3.02
1.94 CD3CN
1.32
1.31
1.00
5.99
1.99
^{1}H chemical shift (ppm)

(b2)

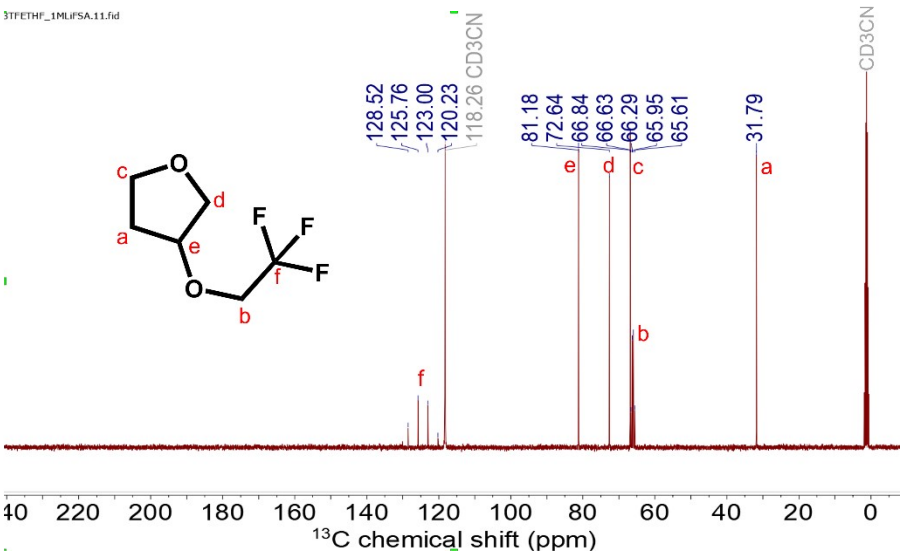
3TFETHF_1MLiFSA.11.fid
128.52
125.76
123.00
120.23
118.26 CD3CN
81.18
72.64
66.84
66.63
66.29
65.95
65.61
31.79
CD3CN
^{13}C chemical shift (ppm)

(b3)

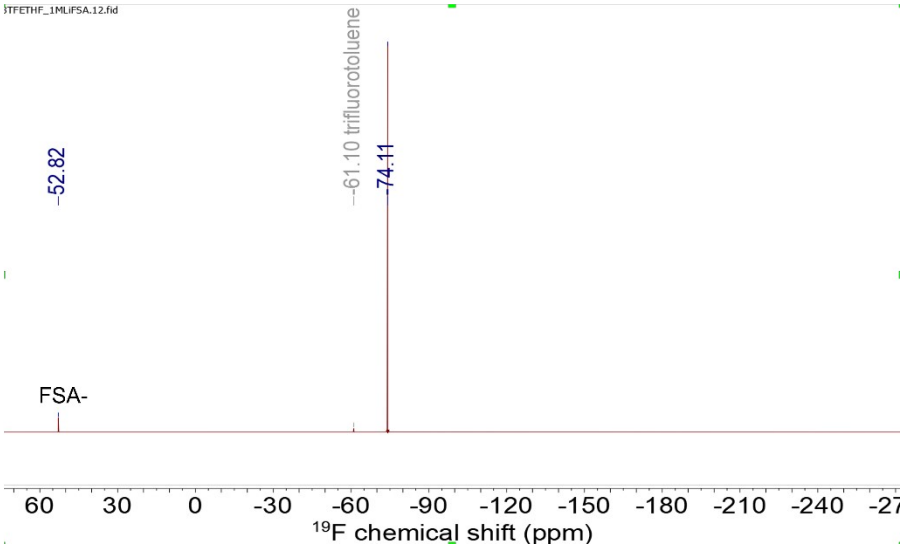
3TFETHF_1MLiFSA.12.fid
-52.82
-61.10 trifluorotoluene
-74.11
FSA-
^{19}F chemical shift (ppm)

(c1)

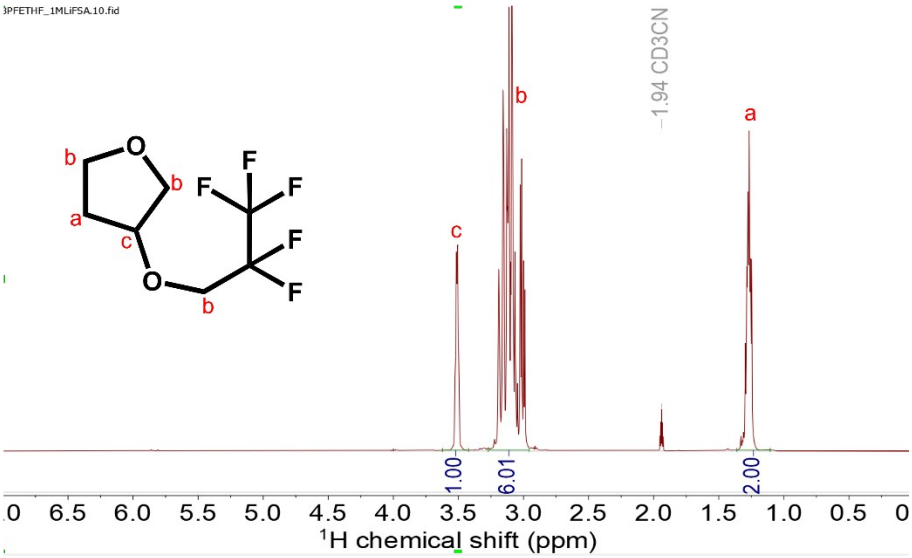
1.94 CD3CN
1.00
6.01
2.00
^{1}H chemical shift (ppm)

(c2)

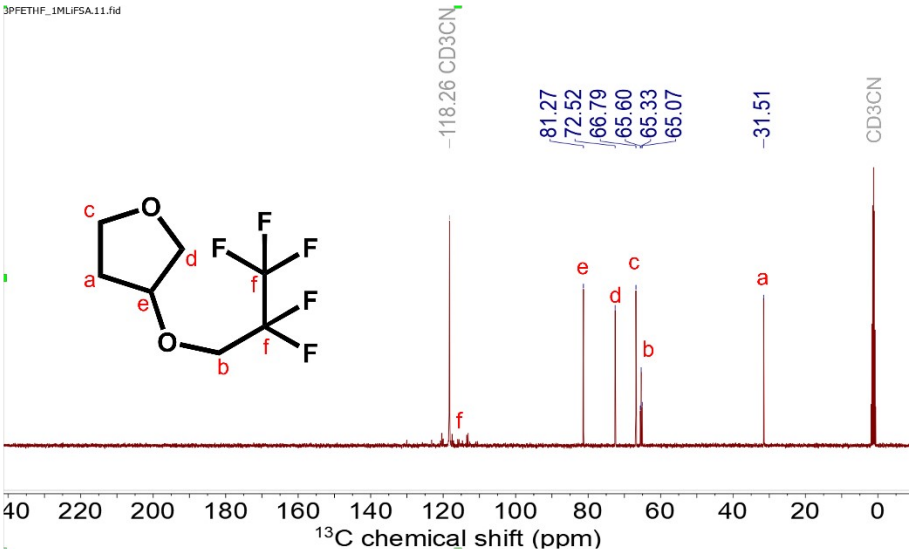
118.26 CD3CN
81.27
72.52
66.79
65.60
65.33
65.07
31.51
CD3CN
^{13}C chemical shift (ppm)

(c3)

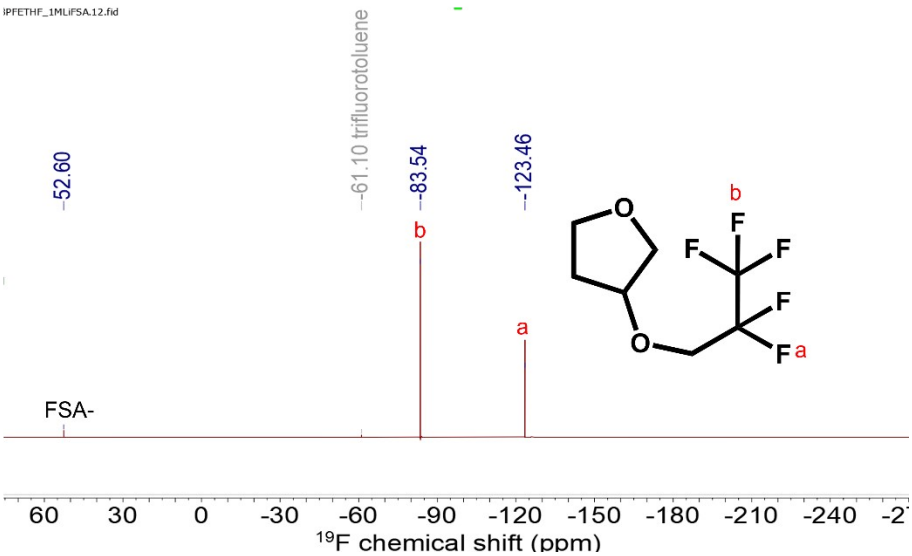
52.60
61.10 trifluorotoluene
83.54
123.46
FSA-
^{19}F chemical shift (ppm)

(d1)

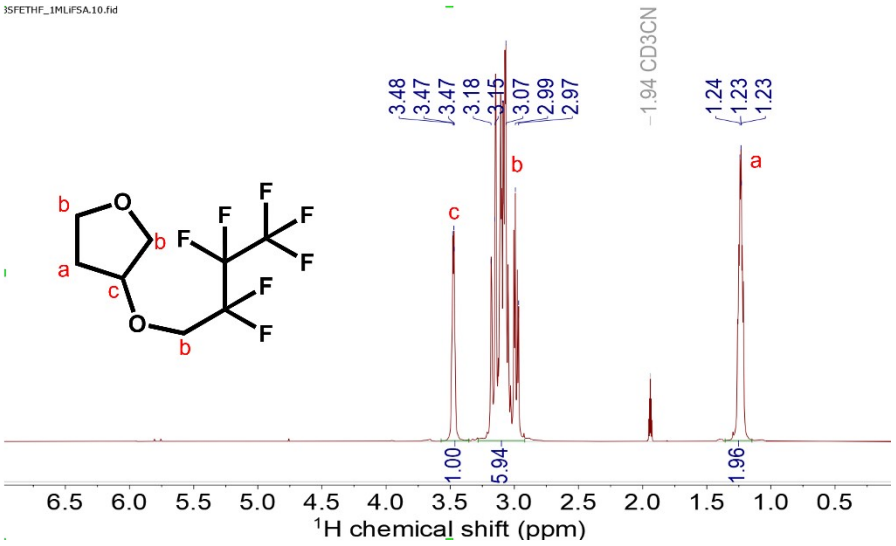
3SFETHF_1MLiFSA.10.fid
3.48
3.47
3.47
3.18
3.15
3.07
2.99
2.97
1.94 CD3CN
1.24
1.23
1.23
1.00
5.94
1.96
6.5 6.0 5.5 5.0 4.5 4.0 3.5 3.0 2.5 2.0 1.5 1.0 0.5
¹H chemical shift (ppm)

(d2)

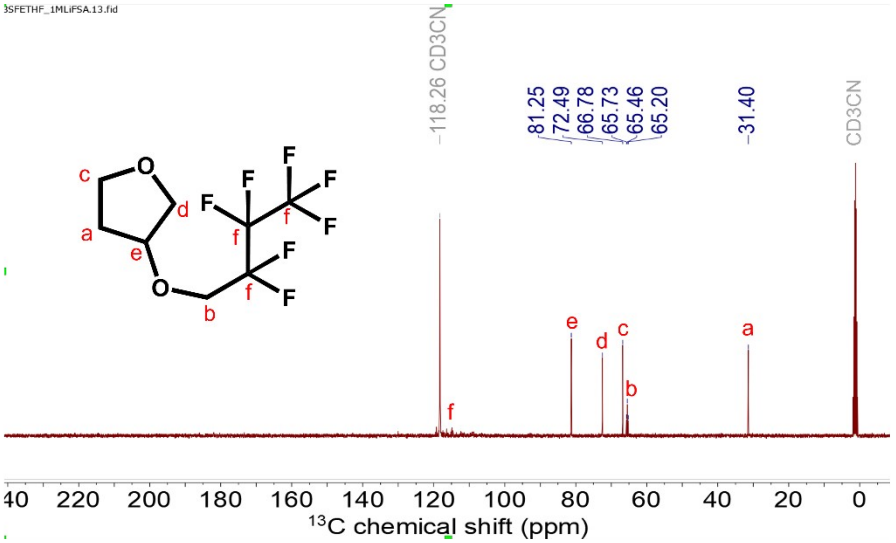
3SFETHF_1MLiFSA.13.fid
118.26 CD3CN
81.25
72.49
66.78
65.73
65.46
65.20
31.40
CD3CN
40 220 200 180 160 140 120 100 80 60 40 20 0
¹³C chemical shift (ppm)

(d3)

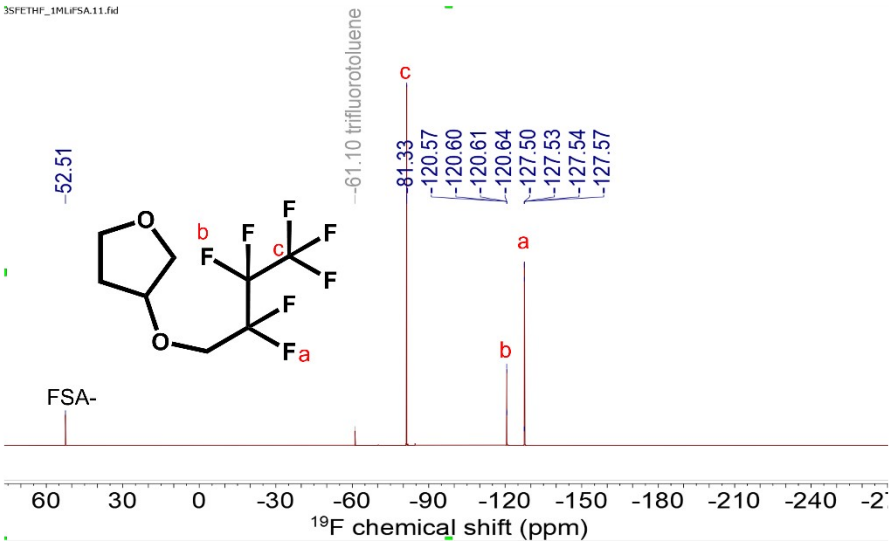
3SFETHF_1MLiFSA.11.fid
61.10 trifluorotoluene
52.51
81.33
120.57
120.60
120.61
120.64
127.50
127.53
127.54
127.57
FSA-
60 30 0 -30 -60 -90 -120 -150 -180 -210 -240 -2
¹⁹F chemical shift (ppm)

(e1)

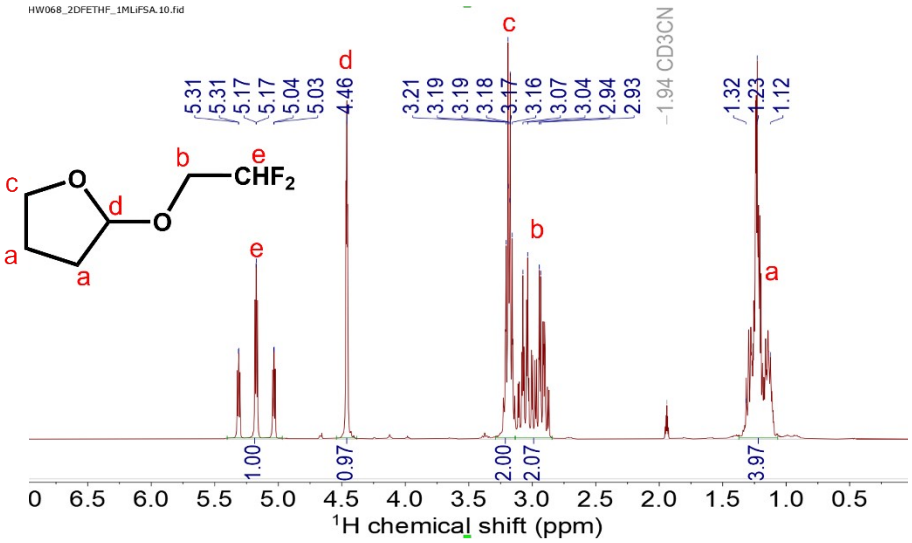
HW068_2DFETHF_1MLiFSA.10.fid
5.31
5.31
5.17
5.17
5.04
5.03
4.46
3.21
3.19
3.19
3.18
3.17
3.16
3.07
3.04
2.94
2.93
1.94 CD3CN
1.32
1.23
1.12
CHF2
1.00
0.97
2.00
2.07
3.97
0 6.5 6.0 5.5 5.0 4.5 4.0 3.5 3.0 2.5 2.0 1.5 1.0 0.5
1H chemical shift (ppm)

(e2)

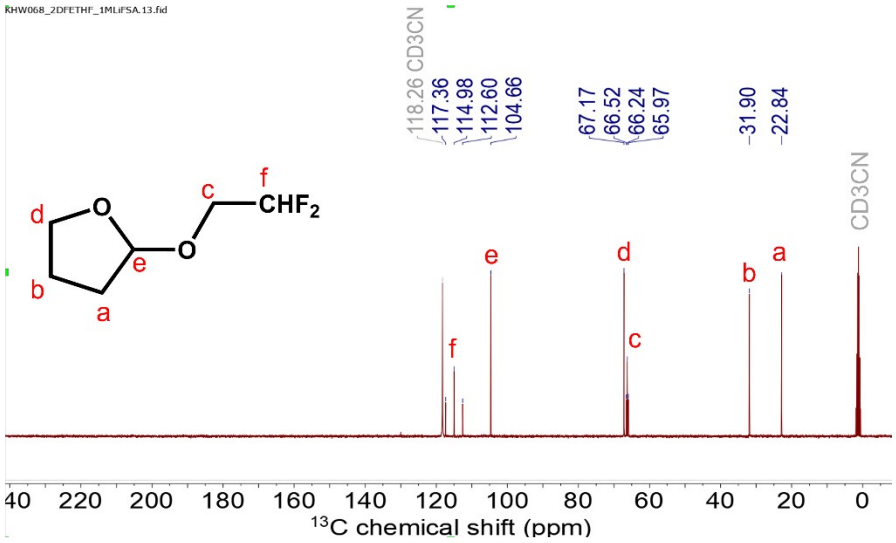
RHW068_2DFETHF_1MLiFSA.13.fid
118.26 CD3CN
117.36
114.98
112.60
104.66
67.17
66.52
66.24
65.97
31.90
22.84
CD3CN
CHF2
40 220 200 180 160 140 120 100 80 60 40 20 0
13C chemical shift (ppm)

(e3)

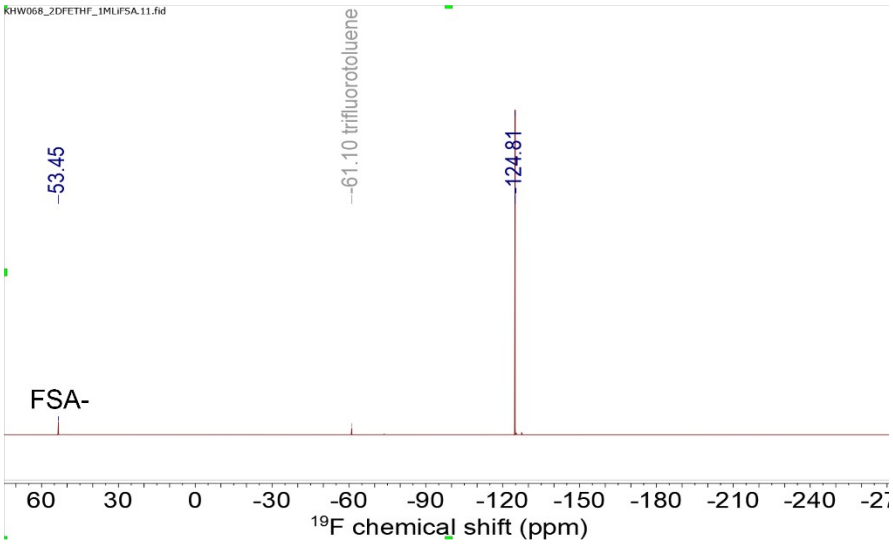
RHW068_2DFETHF_1MLiFSA.11.fid
53.45
61.10 trifluorotoluene
124.81
FSA-
60 30 0 -30 -60 -90 -120 -150 -180 -210 -240
19F chemical shift (ppm)

(f1)

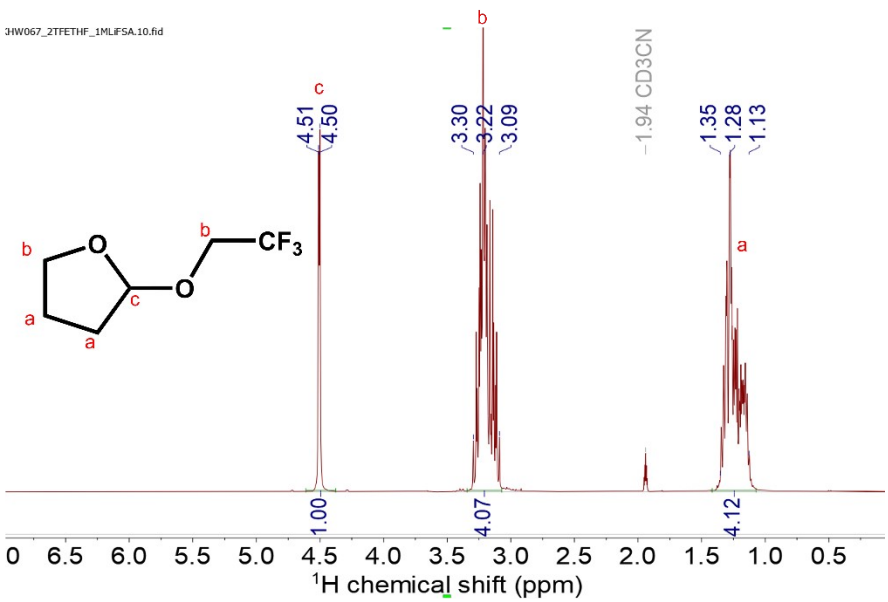
HW067_2TFETHF_1MLiFSA.10.fid
4.51
4.50
3.30
3.22
3.09
1.94 CD3CN
1.35
1.28
1.13
1.00
4.07
4.12
^{1}H chemical shift (ppm)

(f2)

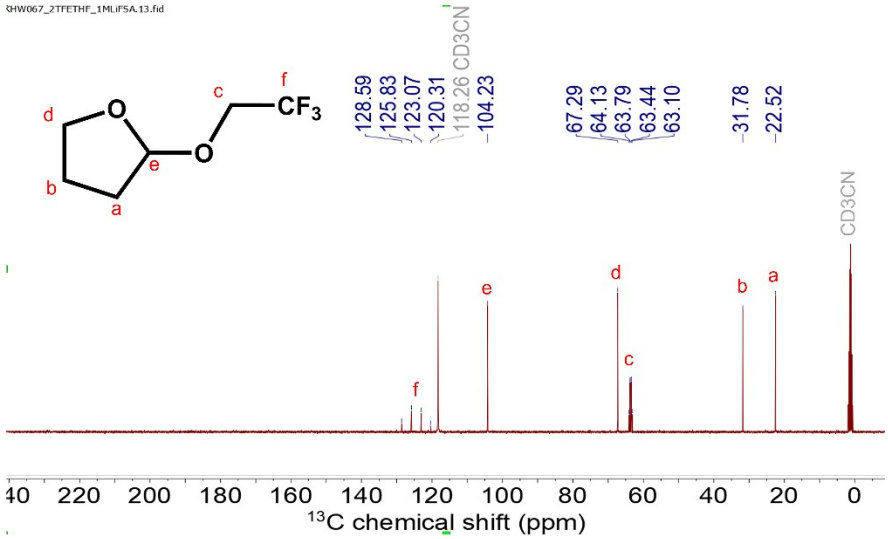
HW067_2TFETHF_1MLiFSA.13.fid
128.59
125.83
123.07
120.31
118.26 CD3CN
104.23
67.29
64.13
63.79
63.44
63.10
31.78
22.52
CD3CN
^{13}C chemical shift (ppm)

(f3)

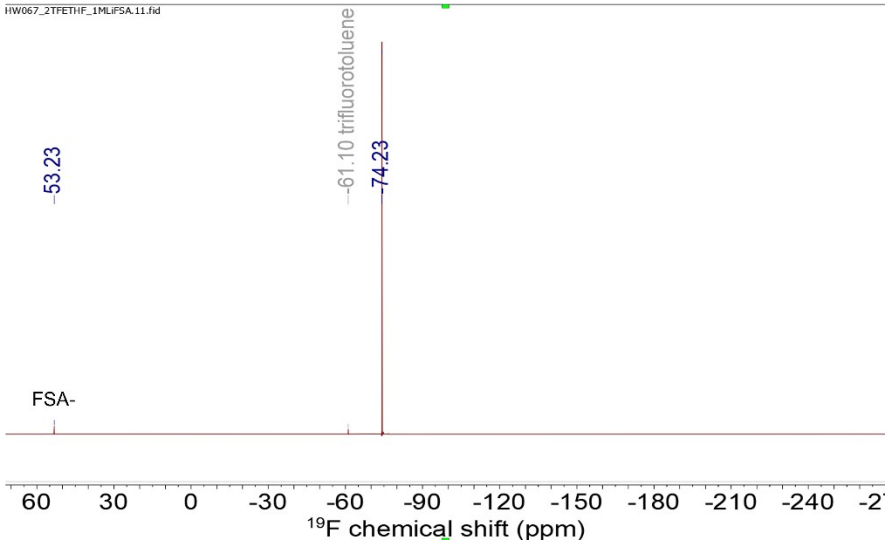
HW067_2TFETHF_1MLiFSA.11.fid
53.23
61.10 trifluorotoluene
74.23
FSA-
^{19}F chemical shift (ppm)

(g1)

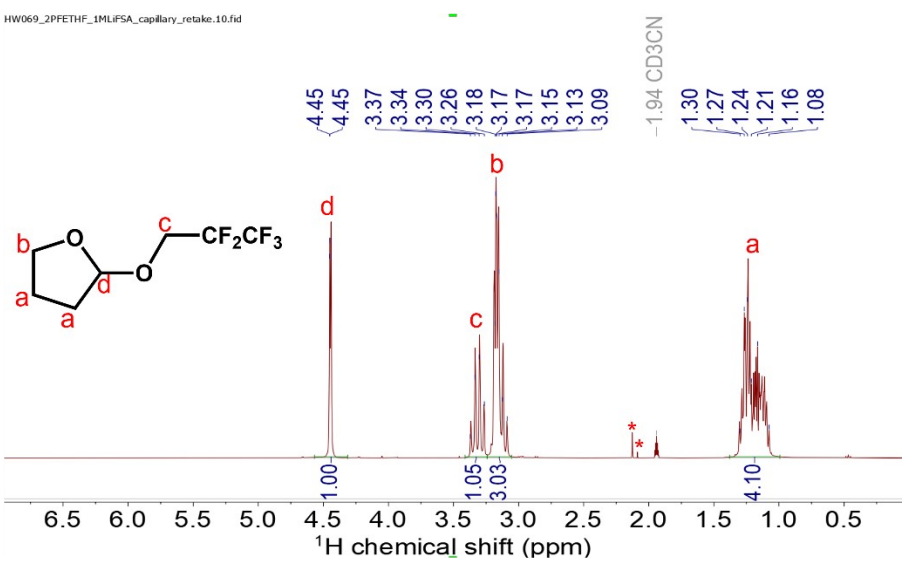
HW069_2PFETHF_1MLiFSA_capillary_retake.10.fid
4.45
4.45
3.37
3.34
3.30
3.26
3.18
3.17
3.17
3.15
3.13
3.09
1.94 CD3CN
1.30
1.27
1.24
1.21
1.16
1.08
b
d
c
a
CF2CF3
1.00
1.05
3.03
4.10
6.5 6.0 5.5 5.0 4.5 4.0 3.5 3.0 2.5 2.0 1.5 1.0 0.5
1H chemical shift (ppm)

(g2)

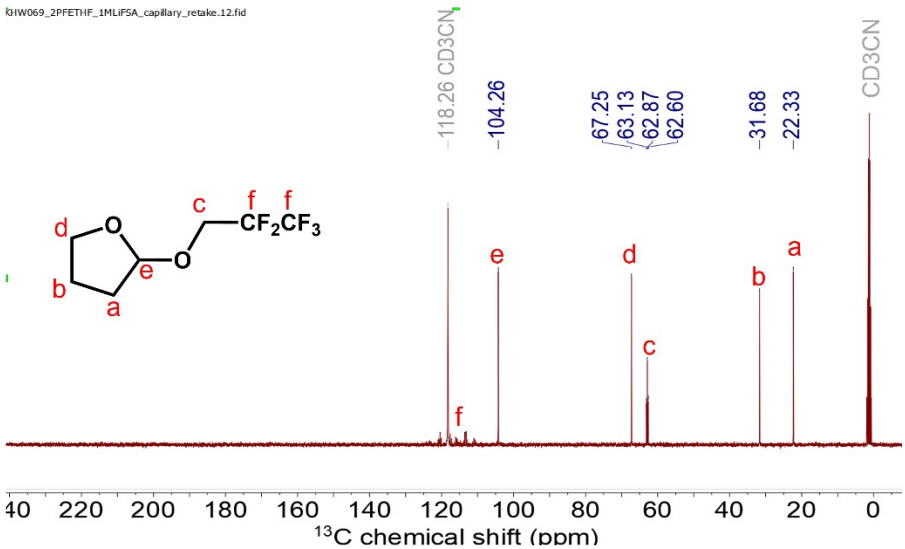
HW069_2PFETHF_1MLiFSA_capillary_retake.12.fid
118.26 CD3CN
104.26
67.25
63.13
62.87
62.60
31.68
22.33
CD3CN
c
f
f
CF2CF3
d
e
b
a
40 220 200 180 160 140 120 100 80 60 40 20 0
13C chemical shift (ppm)

(g3)

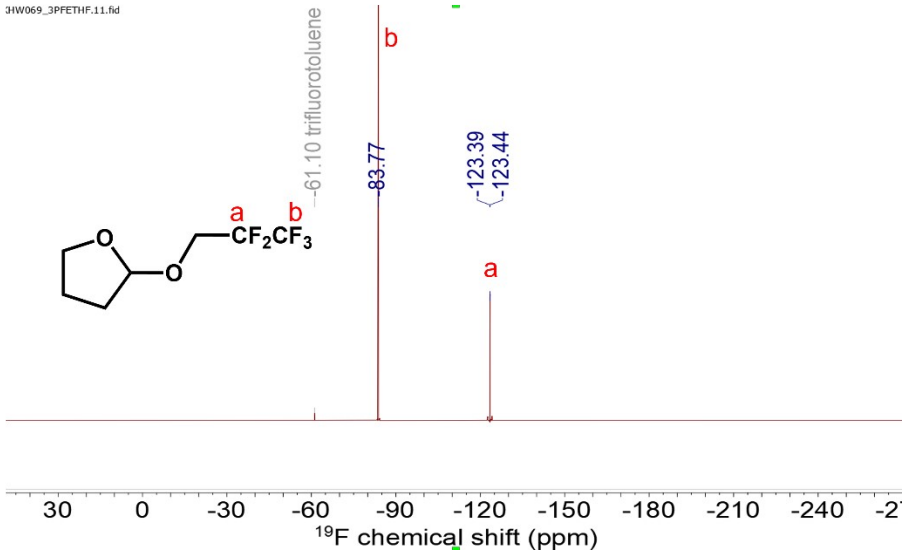
HW069_3PFETHF.11.fid
61.10 trifluorotoluene
b
83.77
123.39
123.44
a
b
CF2CF3
a
30 0 -30 -60 -90 -120 -150 -180 -210 -240
19F chemical shift (ppm)

Figure S2 ^{1}H, ^{13}C, ^{19}F NMR of electrolytes containing fluorinated cyclic ethers and 1 M LiFSA. (**a**) DFETHF (**b**) TFETHF (**c**) PFPTHF (**d**) SFBTHF (**e**) 2DFETHF (**f**) 2TFETHF (**g**) 2PFETHF. Capillary setup is used in this experiment (with electrolyte sample). 0.1 M $LiClO_4$ in CD_3CN with the addition of α,α,α-trifluorotoluene (0.1 %vol of CD_3CN) is the reference solution outside of the capillary. *: impurities from the deuterated solvent.

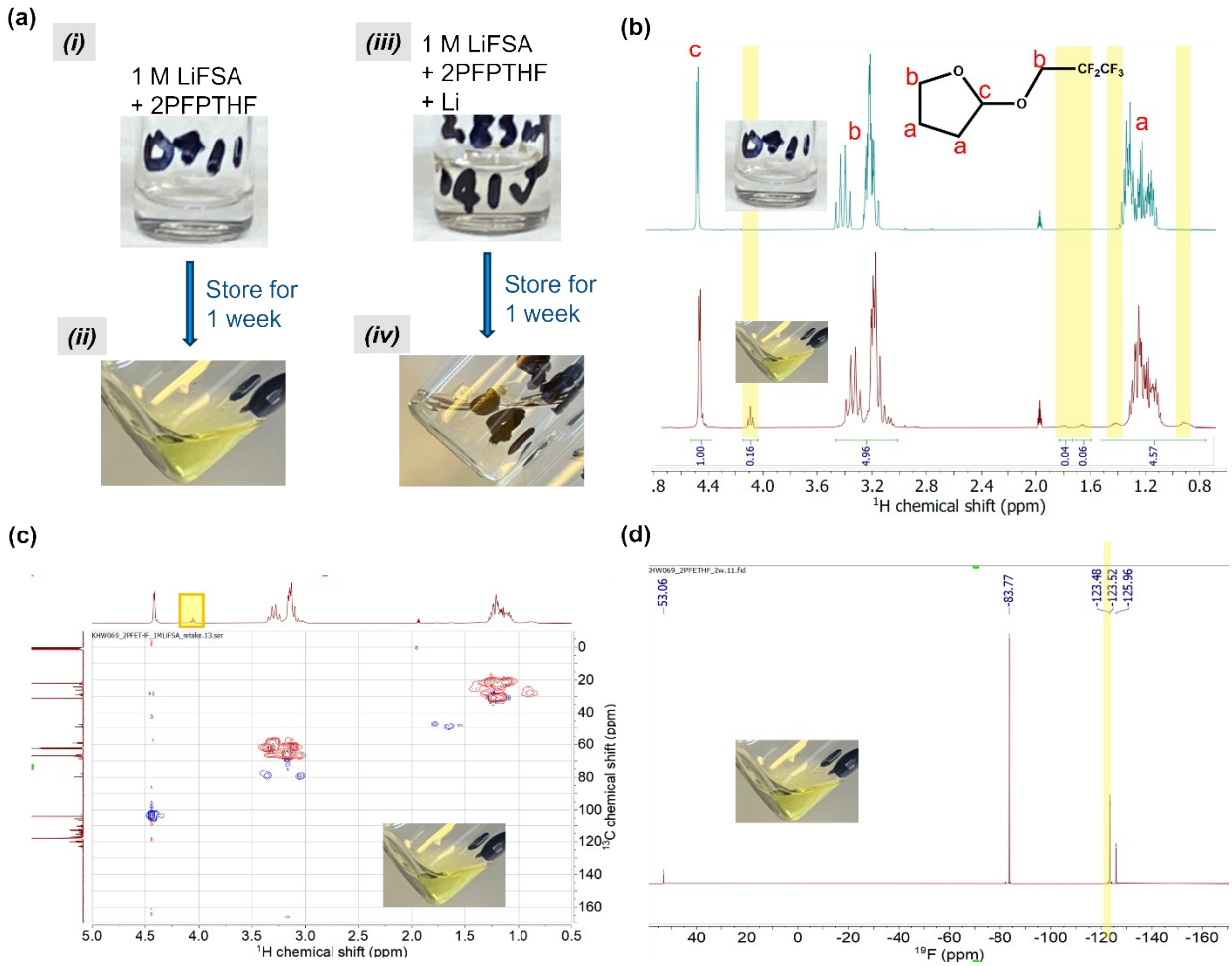

Figure S3 Chemical stability of electrolyte containing 1 M LiFSA in 2'-fluoroalkyl THF. (**a**) Optical images of 1 M LiFSA in 2PFPTHF. *(i)* Fresh solution. *(ii)* 1 M LiFSA in 2PFPTHF solution after being kept for a week in an argon-filled glovebox. *(iii)* 1 M LiFSA in 2PFPTHF with the addition of lithium metal (~1 mg). *(iv)* Lithium metal with 1 M LiFSA in 2PFPTHF after being kept for a week in the glovebox. (**b**) ^{1}H NMR of sample *(i)* and sample *(ii)* in (a). The spectrum on the top refers to sample *(i)*, and the one on the bottom is sample *(ii)*. The yellow box marked the peaks that appeared after storage. Chemical structure of 2FPTHF is shown in **b**. (**c**) 2D-HSQC (Heteronuclear Single Quantum Coherence) spectrum of the sample *(ii)* in Figure a. The yellow box which indicates the peak at 4.1 ppm in ^{1}H NMR spectrum shows the potential presence of –OH. (**d**) ^{19}F NMR of the aged 1 M LiFSA/2PFPTHF solution. The yellow box marks the peak that appeared after 1 week of storage.

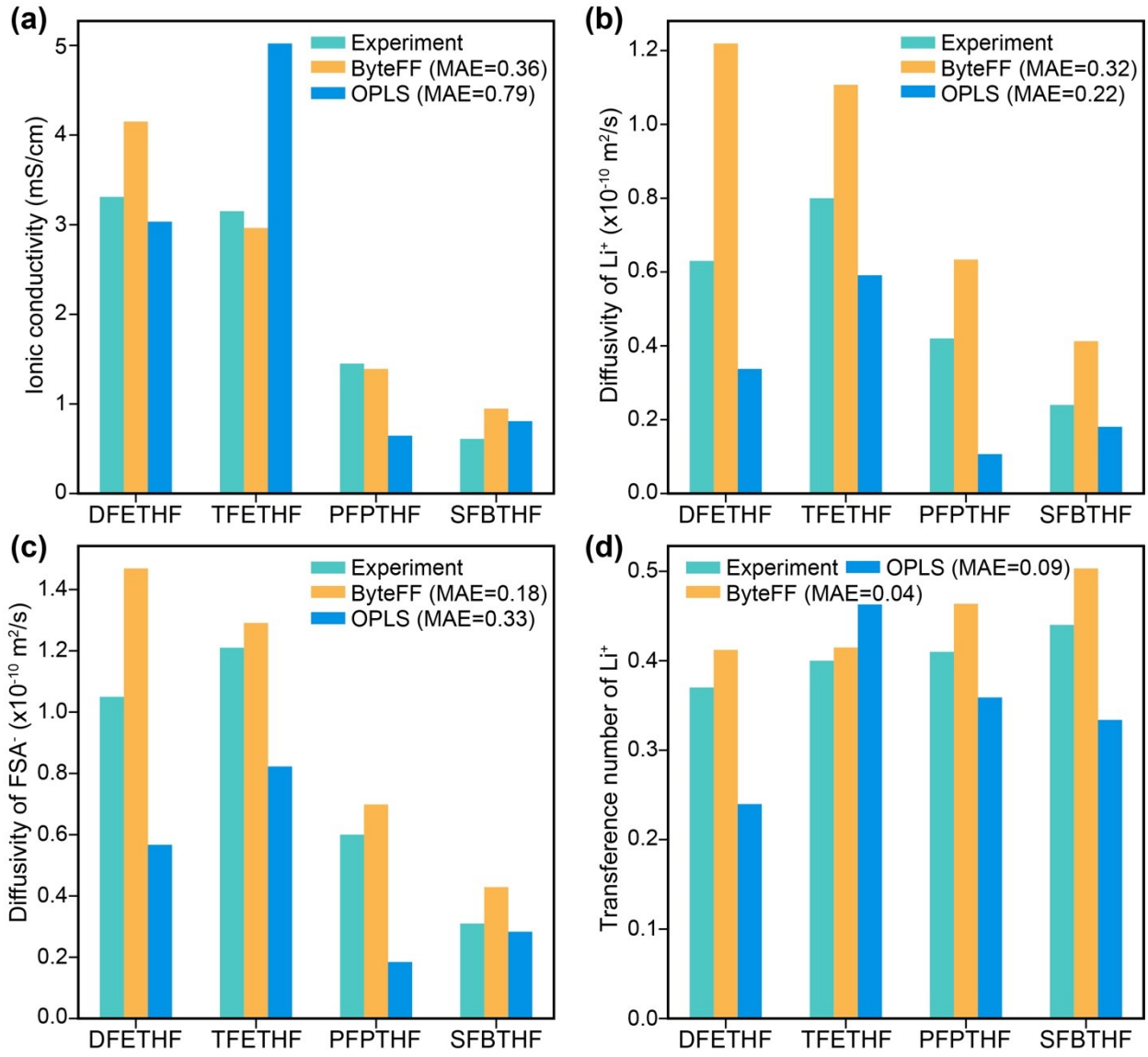

Figure S4 Comparison of polarizable (ByteFF-Pol) and non-polarizable (OPLS) force field-predicted transport properties of liquid electrolytes investigated in the present study. (**a**) Comparison of ionic conductivity. (**b**) Comparison of diffusivity of Li^+ ions. (**c**) Comparison of FSA^- anion, and (**d**) Comparison of transference number of Li^+ ions. MAE = mean absolute error.

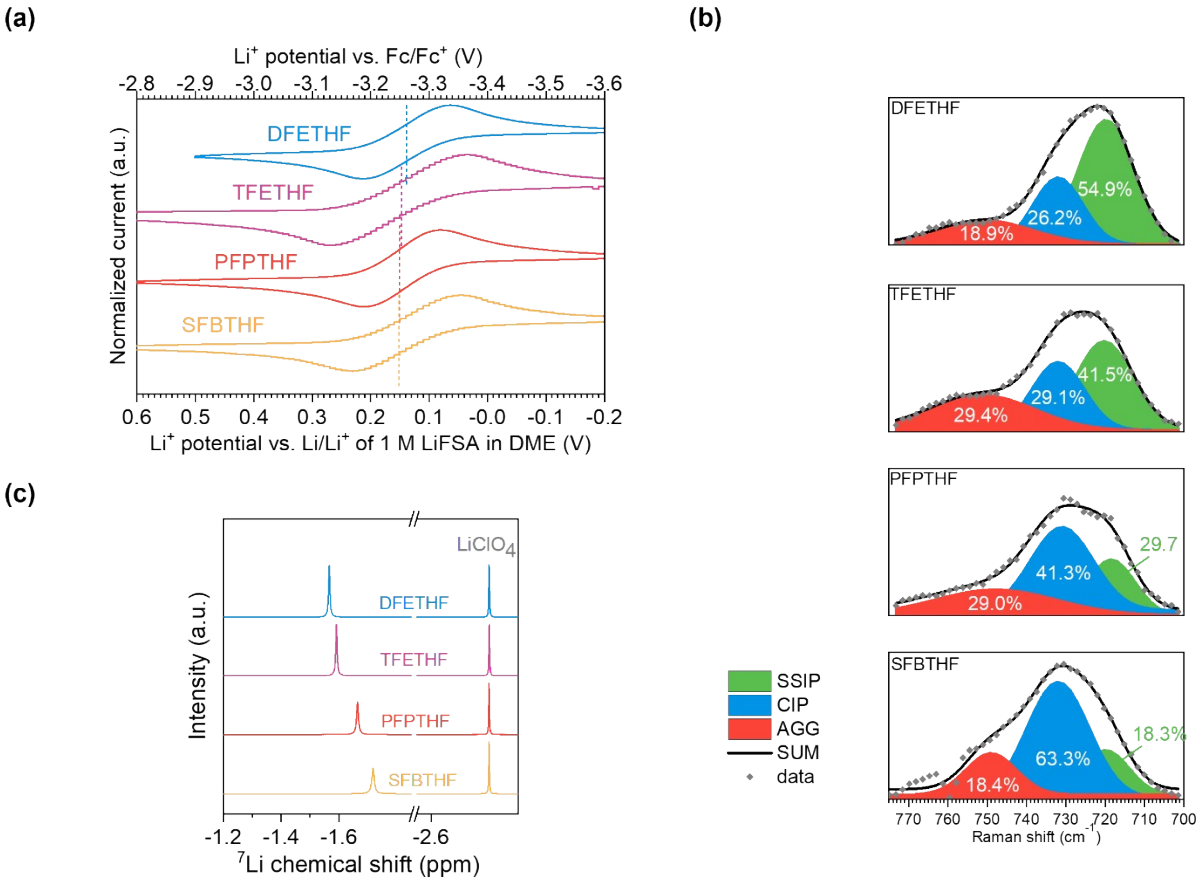

Figure S5 Solvation-related properties of the electrolytes containing 1 M LiFSA in fluorinated cyclic ethers. (**a**) Li^+ potential (E_{Li}) measurement using Fc/Fc^+ as the reference. The method was developed by Ko et al.[20] (**b**) S–N–S stretching of FSA^- probed by Raman spectroscopy. (**c**) ^7Li NMR of the electrolytes. 0.1 M $LiClO_4$ in CD_3CN is used as the reference.

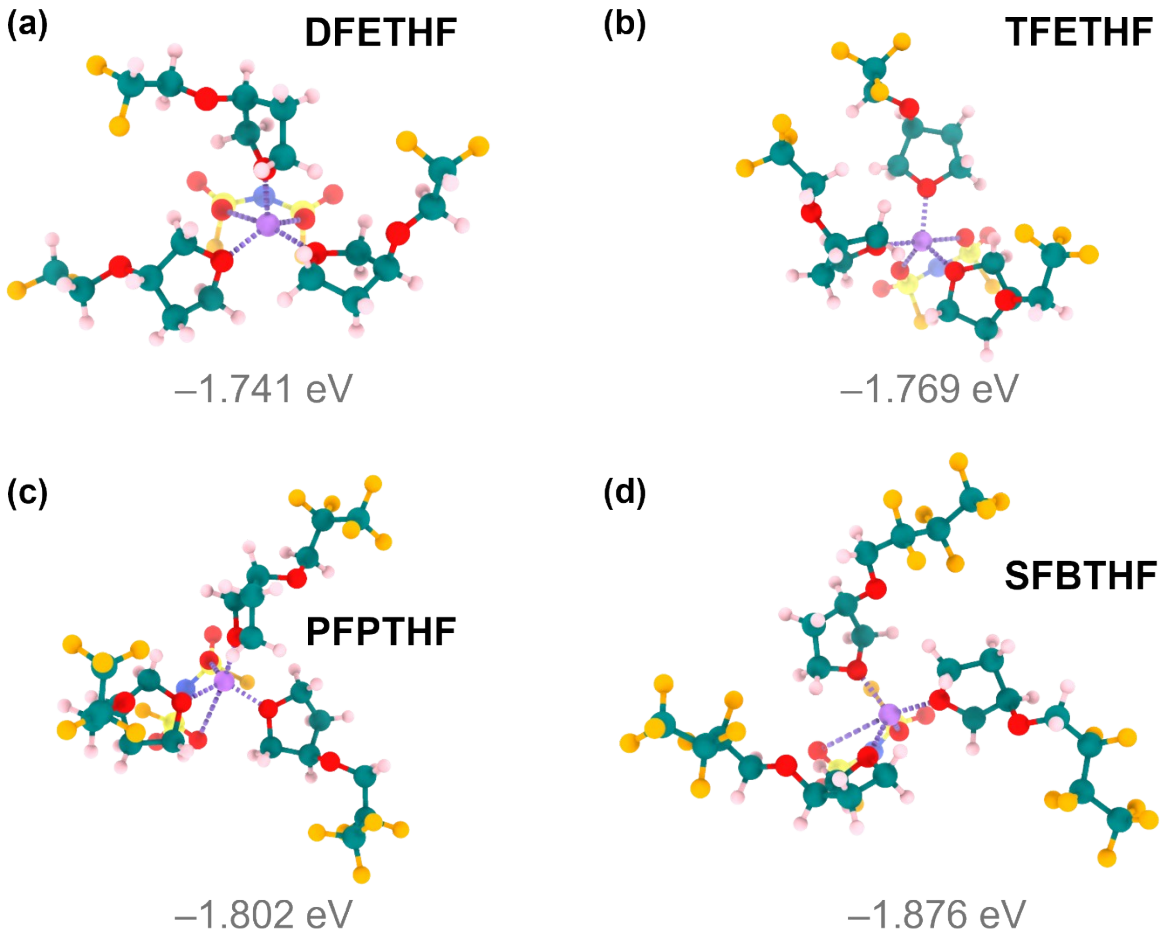

Figure S6 Contact ion pair (CIP) solvation clusters containing 3 solvents and 1 anion bound to a Li^+ ion, extracted from ByteFF-Pol MD and optimized using DFT. (**a**) DFETHF. (**b**) TFETHF. (**c**) PFPTHF. (**d**) SFBTHF electrolytes. The corresponding solvation energy values are shown below each of the structures. Carbon, hydrogen, oxygen, fluorine, nitrogen, sulfur, and lithium atoms are depicted by spheres in teal, pink, red, orange, blue, yellow, and purple colors, respectively. The coordination of atoms on solvents and anions to the Li^+ ion are shown by purple dashed lines.

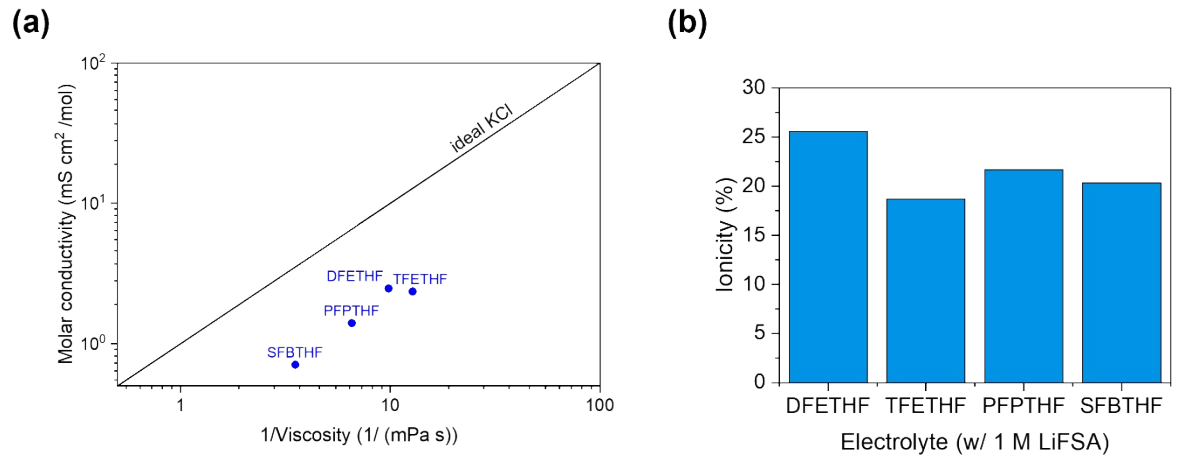

Figure S7 Walden plot and ionicity of fluorinated cyclic ethers extracted from Walden plot.[21, 22] (**a**) Molar conductivity versus the inverse viscosity calculated from values shown in Table S1. The diagonal line in the plot represents the theoretical behavior of 0.01 M KCl aqueous solution where ions are fully dissociated. (**b**) Ionicity derived from ΔW, the distance between ideal line and the individual data point shown in (a). Ionicity values are calculated using the formula below:

$$Ionicity\ (\%) = 10^{-\Delta W} \times 100\%$$

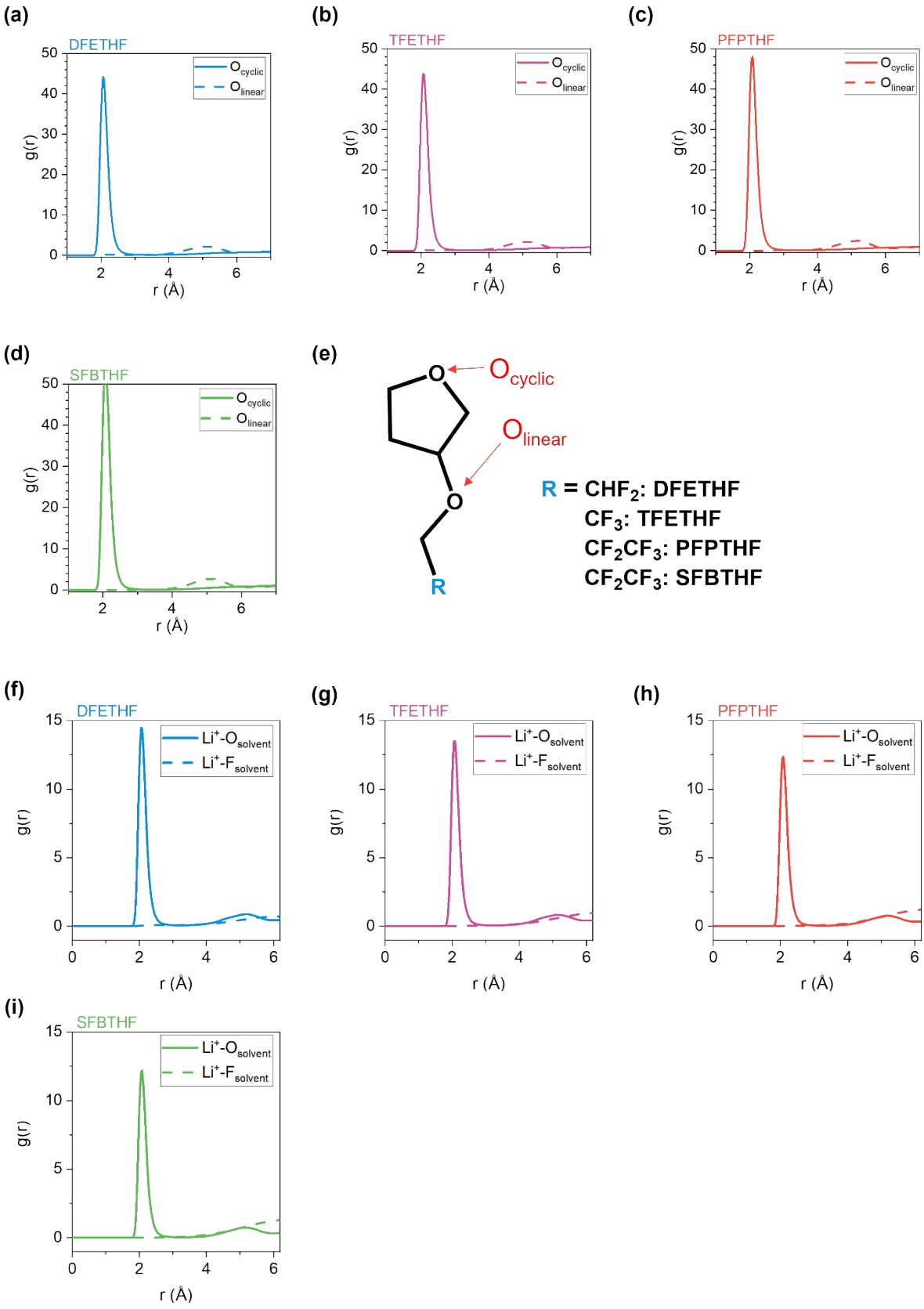
(a)
DFETHF
O_{cyclic}
O_{linear}
g(r)
r (Å)
(b)
TFETHF
(c)
PFPTHF
(d)
SFBTHF
(e)
O_{cyclic}
O_{linear}
R
R = CHF_2: DFETHF
CF_3: TFETHF
CF_2CF_3: PFPTHF
CF_2CF_3: SFBTHF
(f)
DFETHF
Li^+-$O_{solvent}$
Li^+-$F_{solvent}$
(g)
TFETHF
(h)
PFPTHF
(i)
SFBTHF

Figure S8 Classical molecular dynamics (CMD) simulations of fluorinated cyclic ethers with different fluorination degrees using ByteFF-Pol force field. (**a to d**) Radial distribution functions (RDFs) between Li^+ and O_{cyclic} and O_{linear} on the solvent molecule. O_{cyclic} refers to the oxygen atom on the THF ring, and O_{linear} is the oxygen atom connecting the THF ring and the perfluoro chains. (**a**) DFETHF. (**b**) TFETHF. (**c**) PFPTHF. (**d**) SFBTHF. (**e**) A scheme of O_{cyclic} and O_{linear} on the heavily fluorinated solvent molecules. (**f to i**) Normalized RDFs between Li^+ and O (solid line) or F (dashed line) on the solvent molecule. (**f**) DFETHF (**g**) TFETHF (**h**) PFPTHF (**i**) SFBTHF.

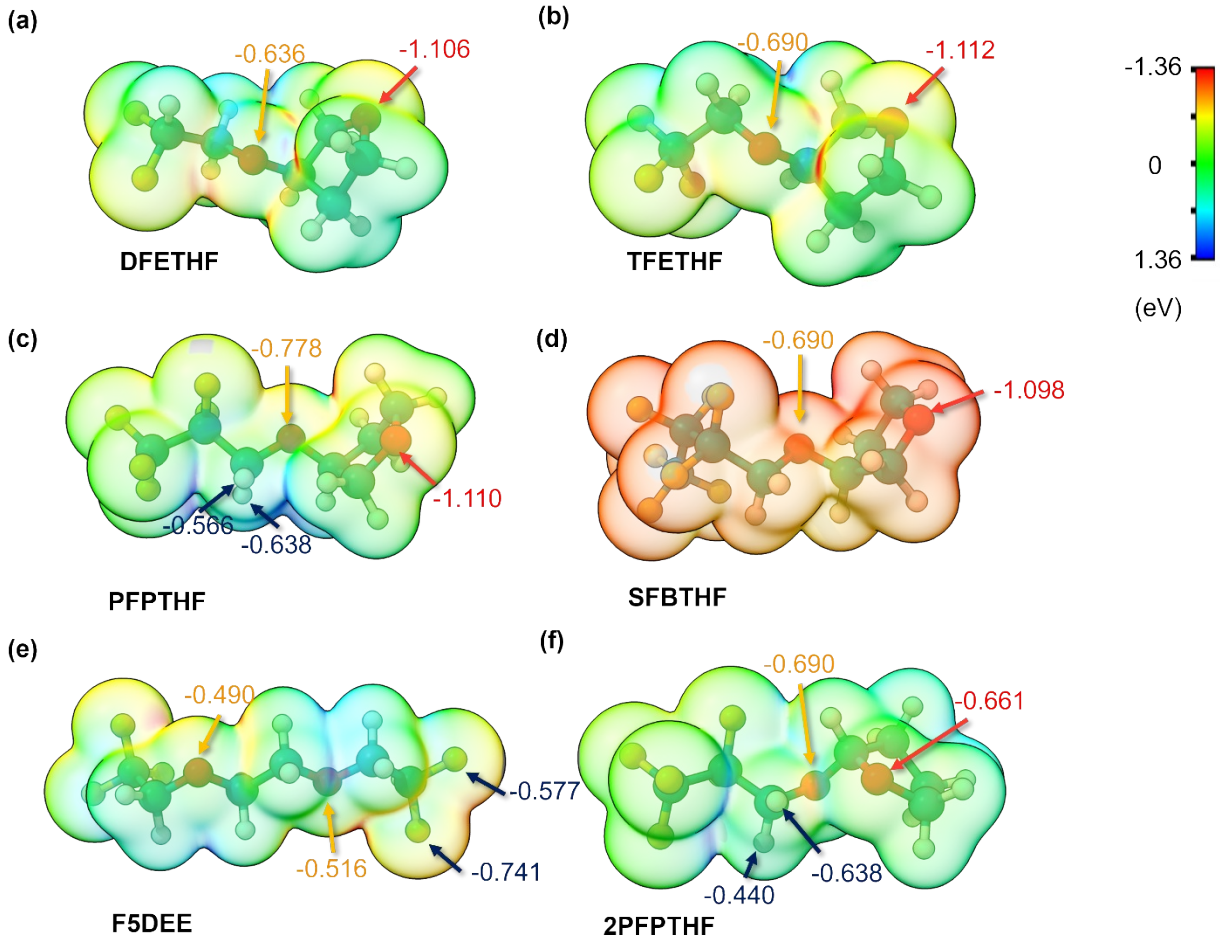

Figure S9 Electrostatic potential (ESP) maps calculated with density functional theory (DFT). ESP values of oxygen atoms on the THF (O_{cyclic}) are labeled with red arrows. Those of other oxygens are labelled with orange arrows. ESP values of fluorine atoms on the molecules containing 5 fluorine atoms are labelled with blue arrows. The unit of labelled ESP values is eV. The surface potential ranges from −1.36 eV (red) to 1.36 eV (blue). (**a**) DFETHF (**b**) TFETHF (**c**) PFPTHF (**d**) SFBTHF (**e**) F5DEE (**f**) 2PFPTHF. Carbon, hydrogen, oxygen, fluorine, nitrogen, sulfur, and lithium atoms are depicted by spheres in teal, pink, red, orange, blue, yellow, and purple colors, respectively. Isosurface value = $5x10^{-3}$ eV / Å^2.

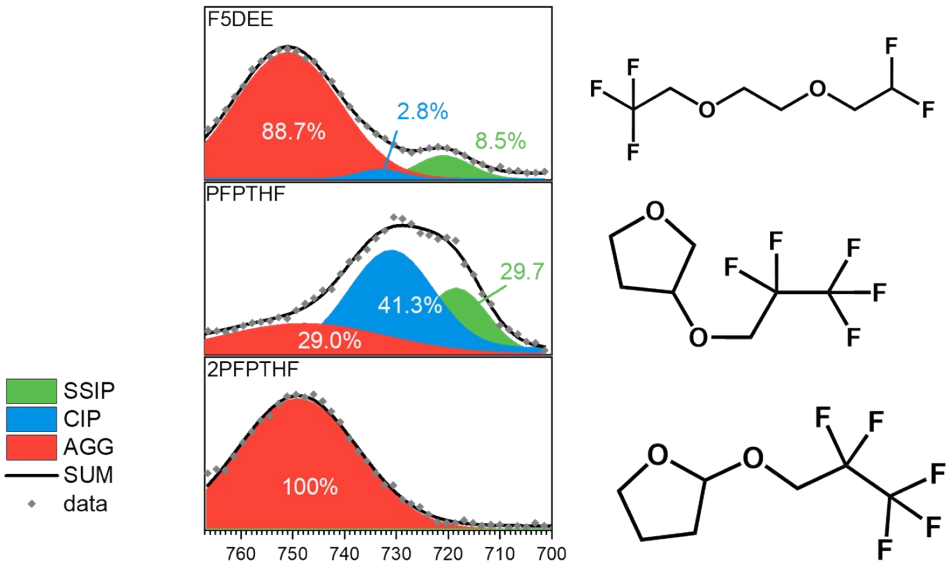

Figure S10 S–N–S stretching of FSA^- in three electrolytes probed by Raman spectroscopy. 1 M LiFSA was used as salt. The molecular structures of the solvent are indicated on the right side of each spectrum. All of them contain 2 oxygen atoms and 5 fluorine atoms.

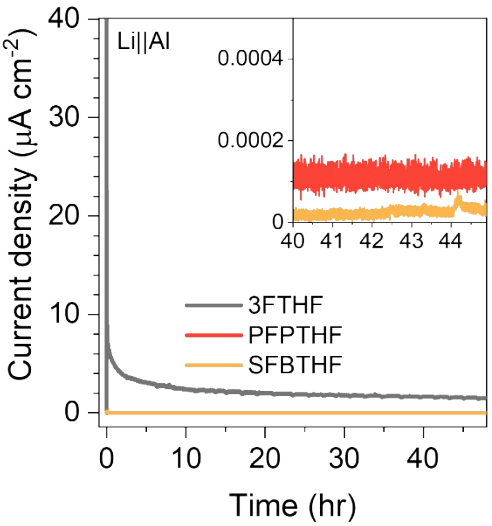

Figure S11 Leakage current of Li||Al cells while the cells were held at 4.4 V. 1 M LiFSA dissolved in three fluorinated cyclic ethers are compared. Inset zooms into the PFPTHF and SFBTHF. Voltage is versus Li/Li^+.

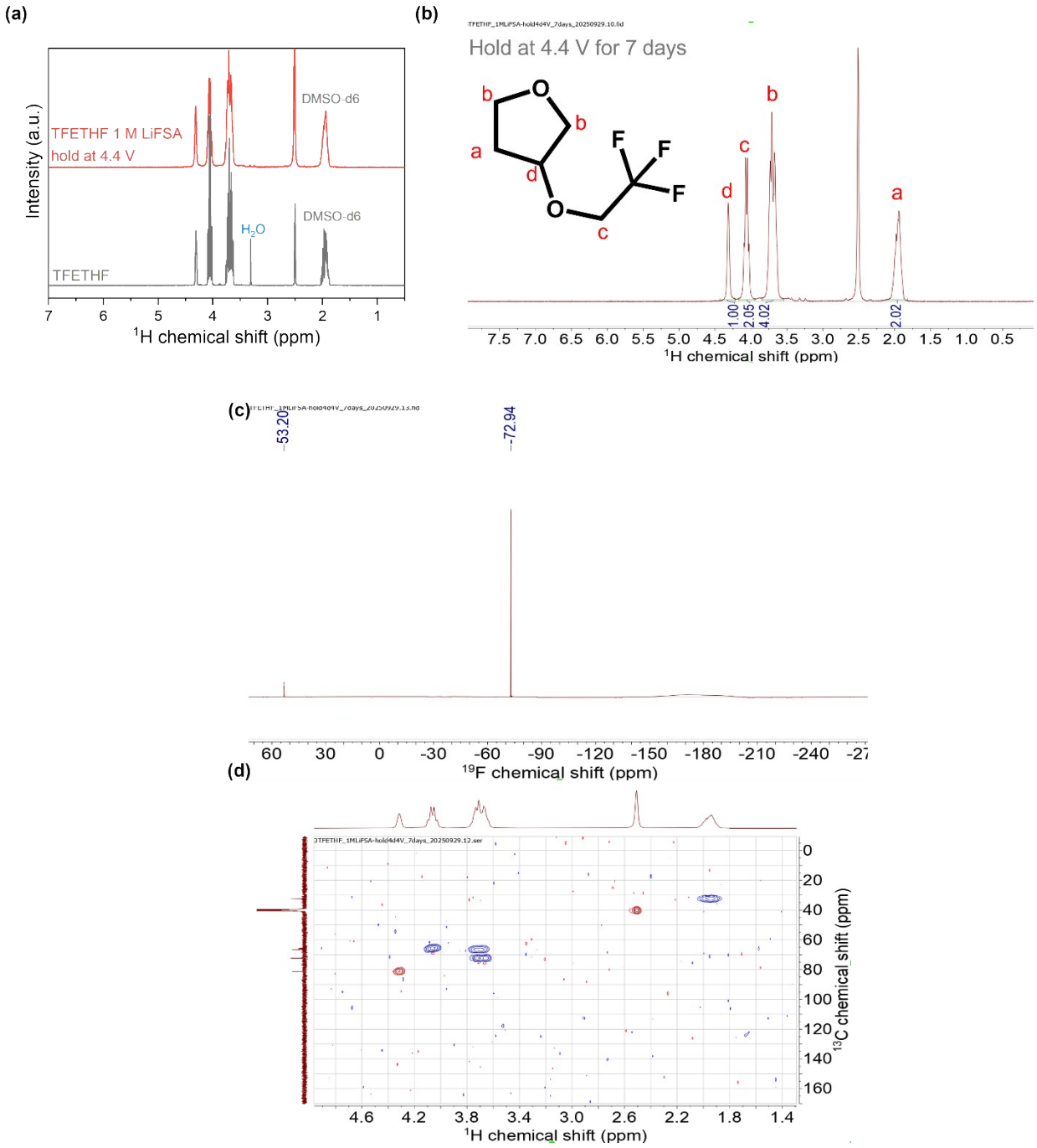

Figure S12 NMR spectra of 1 M LiFSA in TFETHF after holding the Li||Al coin cells containing the electrolyte at 4.4 V (vs. Li/Li$^+$). (**a**) ^{1}H NMR of the electrolyte after holding (red) compared to pristine solvent (gray). (**b**) ^{1}H NMR of the electrolyte (after potentiostatic hold) with the integral of each peak. (**c**) ^{19}F NMR of the electrolyte after potentiostatic hold. (**d**) HSQC of the electrolyte after potentiostatic hold.

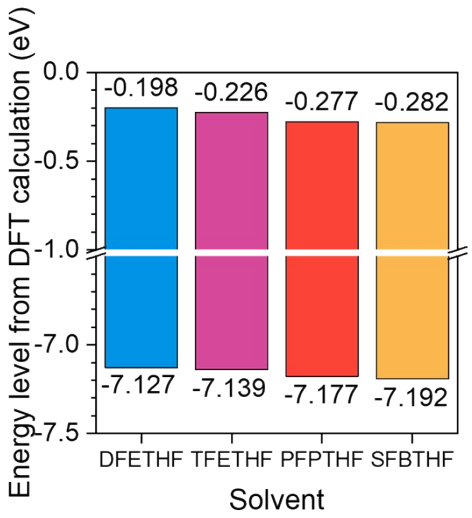

Figure S13 Highest occupied molecular orbital (HOMO) and lowest unoccupied molecular orbital (LUMO) of solvent studied in this work.

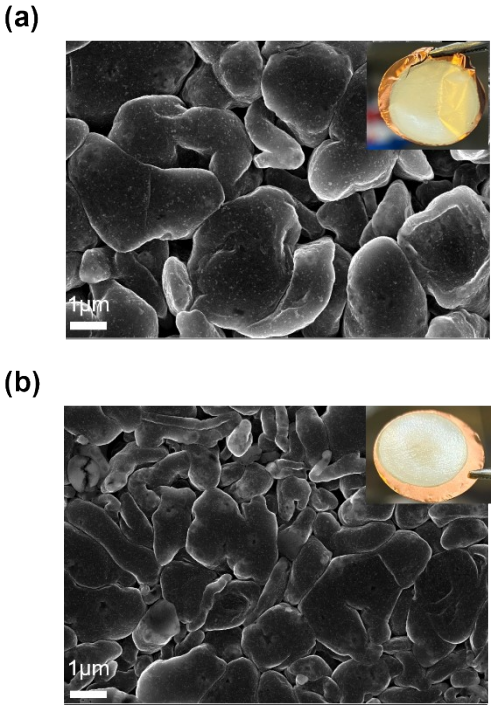

Figure S14 Scanning electron microscopy (SEM) images of Li deposition on Cu. (**a**) 1 M LiFSA in DFETHF. (**b**) 1 M LiFSA in PFPTHF. Li is deposited in a Li||Cu half cell using a current density of 0.5 mA/cm^2 to 1.5 mA h/cm^2. The insets in both figures are digital photographs of the deposited lithium.

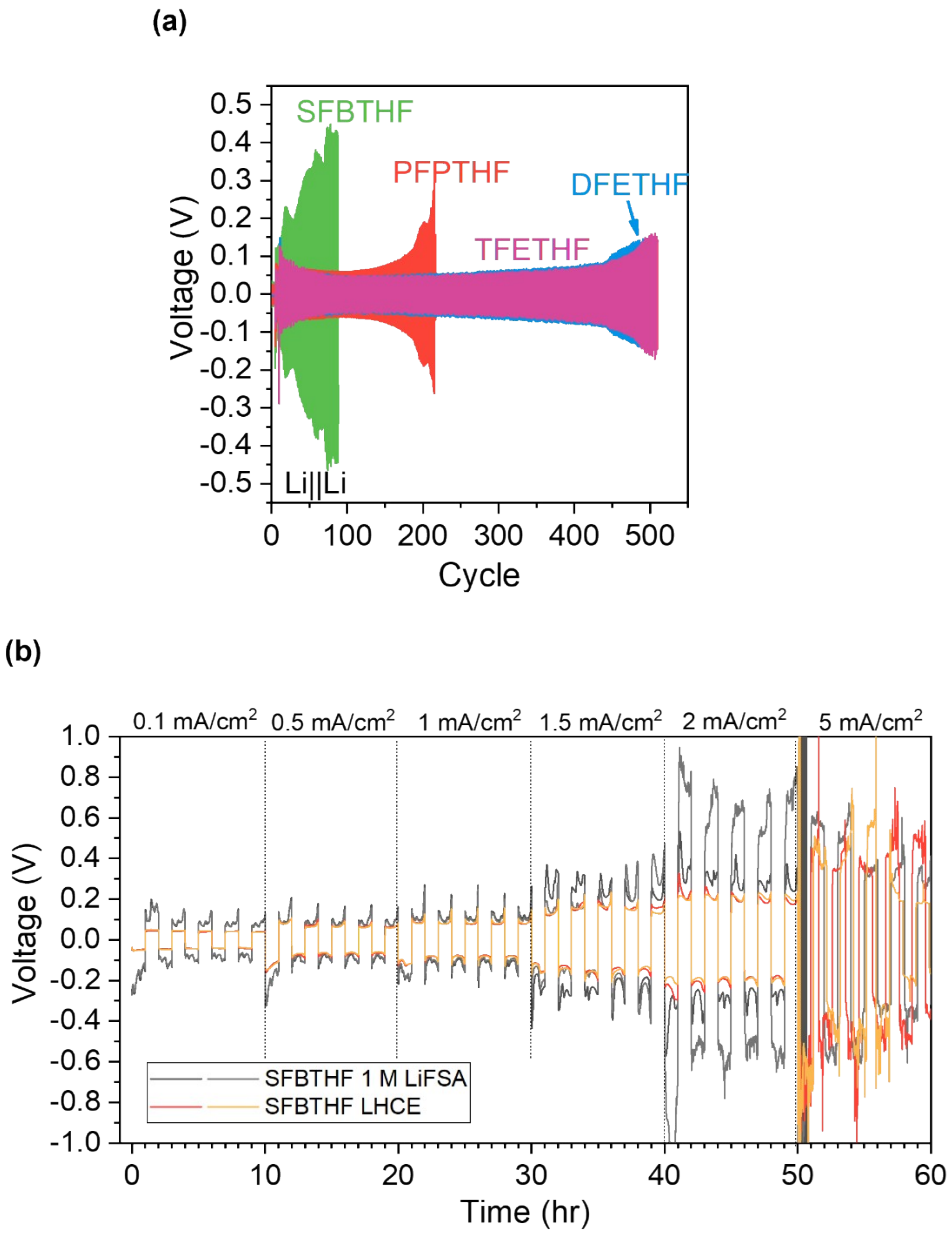

Figure S15 Voltage versus cycle plot of Li||Li symmetric cells. (**a**) Longterm cycling of Li||Li cells at 1 mA/cm^2 to 1 mA h/cm^2 after five formation cycles at 0.02 mA/cm^2 to 0.1 mA h/cm^2. 1 M LiFSA in fluoroalkyl cyclic ethers are used as the electrolytes. (**b**) Critical current density test of electrolytes using SFBTHF as the main solvent. The cells were cycled for 1 hr for each current density indicated in the text above the figure. LHCE: localized high concentration electrolyte composed of SFBTHF, TTE, and LiFSA (molar ratio 1.2:1:1).

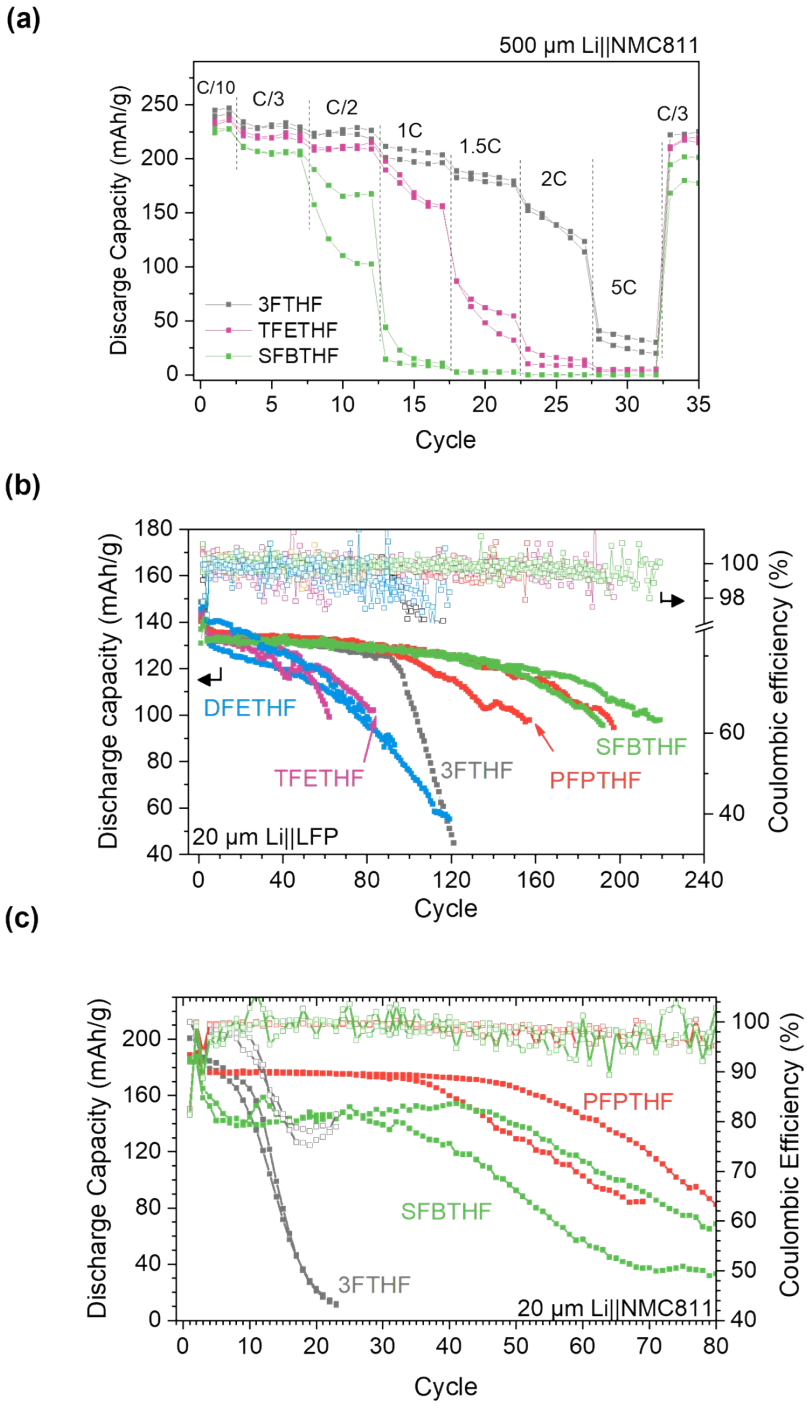

Figure S16 Rate compatibility of high voltage cathode and full cell cycling. (**a**) Rate capability of 500 μm Li||NMC811 cells using representative electrolytes. Cells were cycled at the rate indicated right above data points in the figure. (**b**) Galvanostatic cycling of 20 μm Li||LFP full cell at C/3 (≈ 0.62 mA/cm^2). (**c**) Galvanostatic cycling of 20 μm Li||NMC811 full cell at C/3 (≈ 0.55 mA/cm^2). Replicates of each electrolyte are shown. LFP: $LiFePO_4$. NMC811: $LiNi_{0.8}Mn_{0.1}Co_{0.1}O_2$. NMC811 loading ≈ 1.66 mA h/cm^2. LFP loading ≈ 1.86 mA h/cm^2. Voltage is vs. Li/Li$^+$.

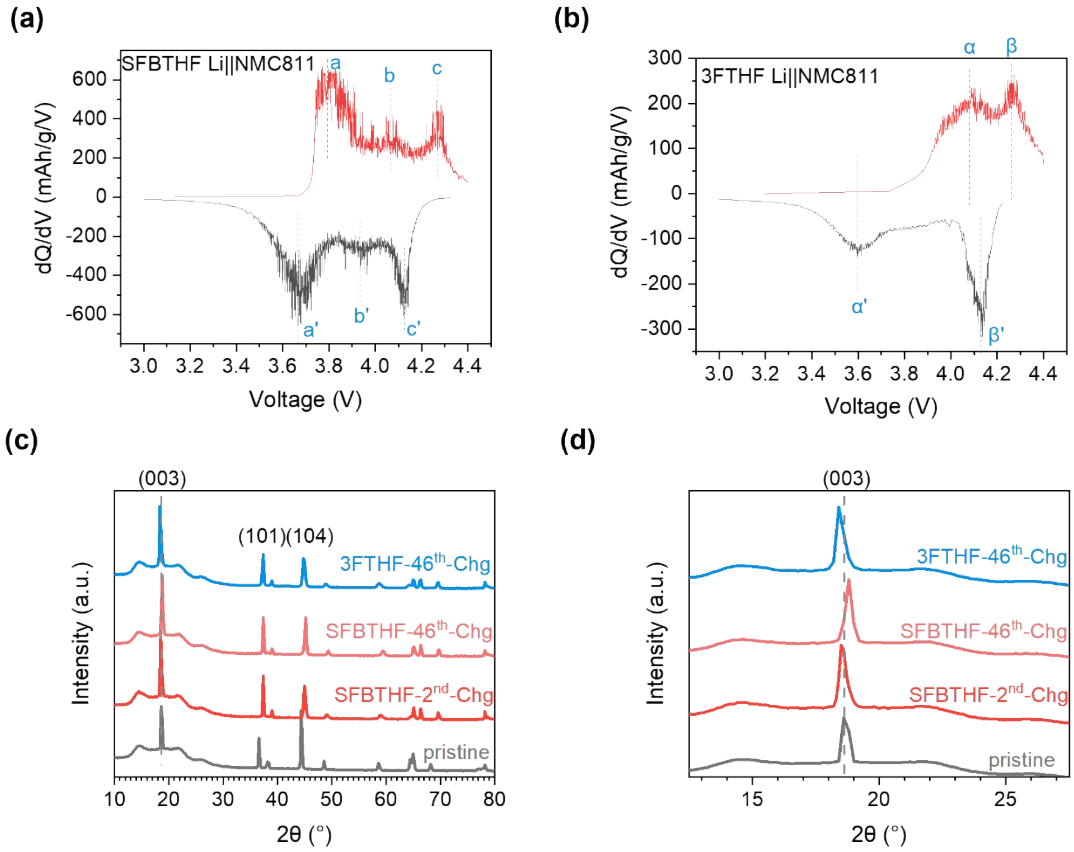

Figure S17 Cathode characterization for Li||NMC811 cells using 1 M LiFSA in 3FTHF or SFBTHF electrolytes. After 2 precycles at C/10, cells were cycled at C/3 (≈ 0.55 mA/cm^2) for 44 cycles and finally charged to 4.4 V prior to analysis. NMC811: $LiNi_{0.8}Mn_{0.1}Co_{0.1}O_2$. NMC811 loading ≈ 1.66 mA h/cm^2. Voltages are vs. Li/Li$^+$. (**a**) dQ/dV profile of the final cycle of Li||NMC811 cell of SFBTHF. (**b**) dQ/dV plot of the final cycle of Li||NMC811 cell of 3FTHF. Red and gray curves correspond to charging (47th half cycle) and discharging (46th half cycle), respectively. (**c**) X-ray diffraction pattern of NMC811 from 10 to 80 degrees. (**d**) Enlarged plot of Figure c focusing on the (003) peaks. Dashed lines are included as guides to the eye. Note that charging is the 'delithiated' state.

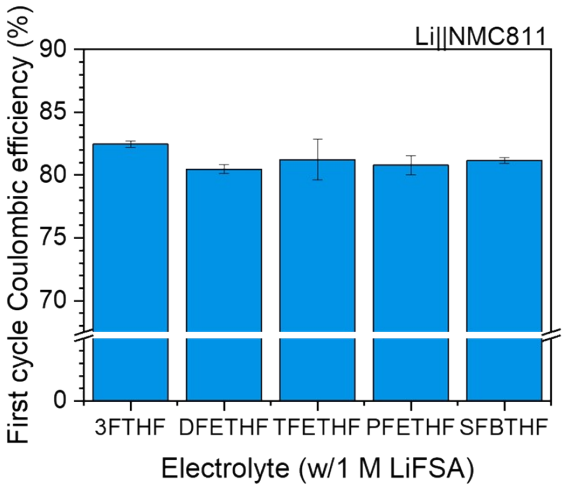

Figure S18 Initial Coulombic efficiencies (CE) of Li||NMC811 cells shown in Figure 4c in the main manuscript. The values represent the average of two cells.

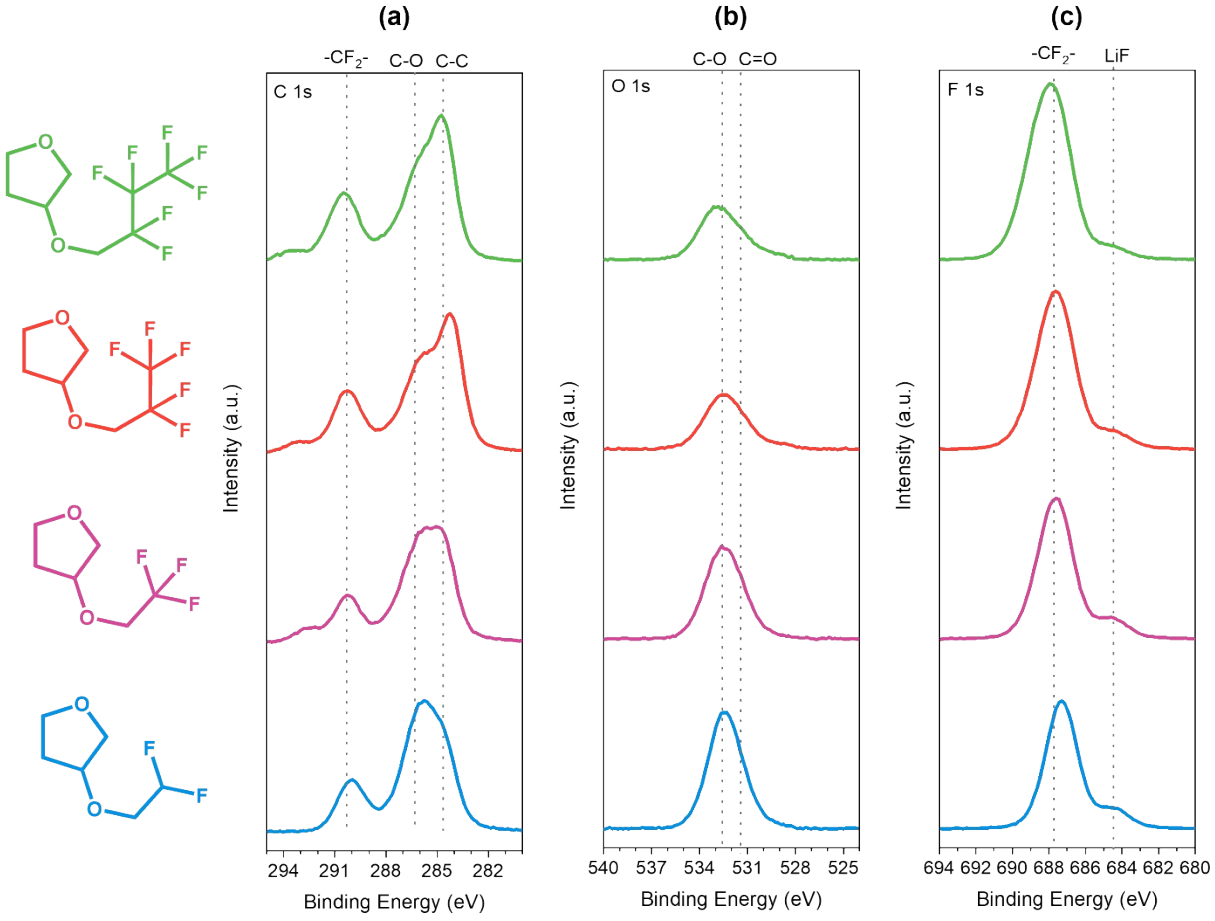

Figure S19 X-ray photoelectron spectroscopy (XPS) of NMC811 cathode after 100 cycles in Li||NMC811 cells. (**a**) C 1s spectra at the surface (**b**) O 1s spectra at the surface (**c**) F 1s spectra at the surface.

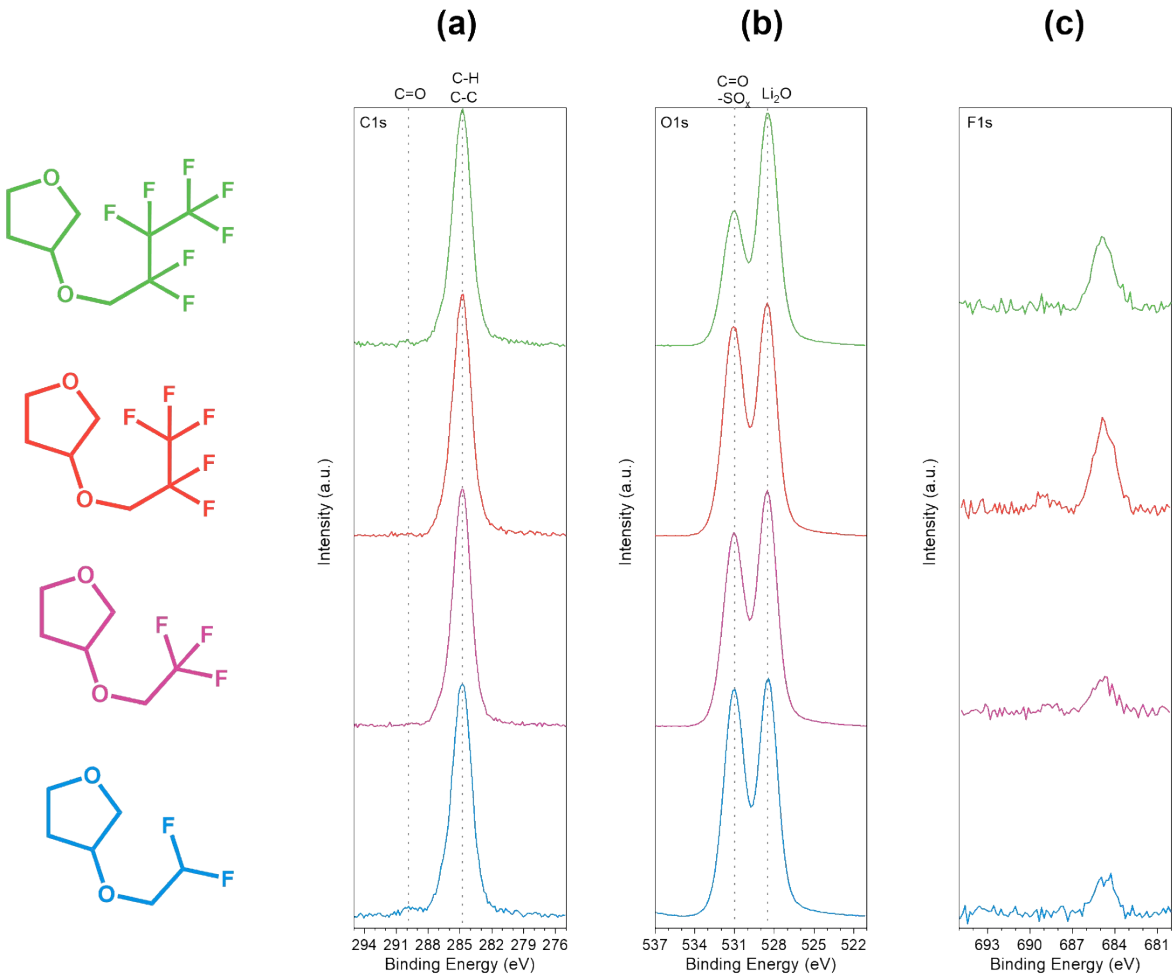

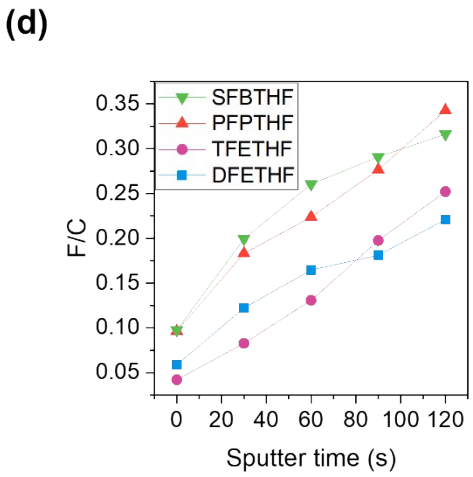

Figure S20 X-ray photoelectron spectroscopy (XPS) of Li electrodeposits in Li||Cu cells. (**a**) C 1s spectra at the surface (**b**) O 1s spectra at the surface (**c**) F 1s spectra at the surface (**d**) Atomic F/C ratio of samples at the surface (sputter time = 0) to the depth after 120 s sputtering using 4 fluorinated ethers as the electrolyte.

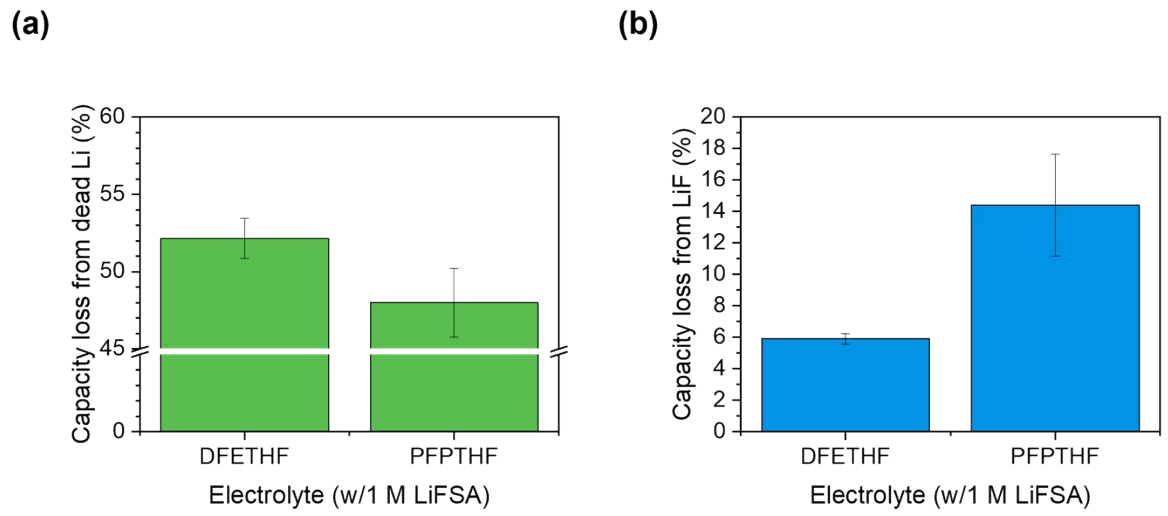

Figure S21 SEI composition quantified by titration method. (**a**) The percentage of capacity loss from dead Li in SEI averaged over two Li||Cu cells. Dead Li was quantified with acid titration. (**b**) The percentage of capacity loss from LiF in SEI averaged over three Li||Cu cells. LiF is quantified with ^{19}F NMR spectroscopy using 2-difluoroethanol as the internal standard. Li||Cu cells were cycled for 5 times at 0.5 mA/cm^2 to 1.5 mAh/cm^2 before titration.

Table S1 Physicochemical properties of the electrolytes discussed in this work. The solvent density, viscosity, and conductivity in this table are measured at room temperature (298K)

Solvent	DFETHF	TFETHF	PFPTHF	SFBTHF
Salt	1 M LiFSA	1 M LiFSA	1 M LiFSA	1 M LiFSA
Solvent density (g/mL)	1.198	1.225	1.326	1.410
Solvent viscosity (mPa s)	2.44	1.68	2.25	3.12
Solvent boiling point at 1 atm*[1] (°C)	178.9	157.2	163.7	167.8
Viscosity of solution (mPa s)	10.18	7.83	15.25	28.34
Conductivity*[2] of solution (mS/cm)	3.31	3.15	1.45	0.61
Conductivity with swelled separator (mS/cm)	0.289	0.275	0.127	0.053

*[1] Estimated from Pressure-Temperature Nomograph Interactive Tool: https://www.sigmaaldrich.com/chemistry/solvents/learningcenter/nomograph.html?gclid=CjwKCAjw9rDBhBxEiwA9qYUpctOuvLP40XzFVLCoWHjYl6vEho6xQ1V2uNm3QzJUdEsakSbSvpuOxoCsFoQAvD_BwE

*[2] Calibrated by cell constant = 11.45

Table S2 Transport properties of the electrolytes discussed in this work. Diffusivities and transference numbers were measured by PFG-NMR.

Solvent	DFETHF	TFETHF	PFPTHF	SFBTHF
Salt	1 M LiFSA	1 M LiFSA	1 M LiFSA	1 M LiFSA
D_{Li+} (10^{-10} m^2/s)	0.63	0.80	0.42	0.24
D_{FSA-} (10^{-10} m^2/s)	1.05	1.21	0.60	0.31
t_+	0.37	0.40	0.41	0.44

Table S3 Solvation and transport properties comparison between 3FTHF and DFETHF. Data of 3FTHF are extracted from previous work.[1]

	Solvation properties			Transport properties	
Electrolyte	E_{Li} (V versus Fc/Fc^+)	^7Li (ppm)	C_m of FSA^- Raman peak (cm^{-1})	t_+	σ (mS/cm)
1 M LiFSA in 3FTHF	-3.276	-1.30	727.2	0.43	8.04
1 M LiFSA in DFETHF	-3.261	-1.36	728.7	0.37	3.31

Table S4 Details of MD simulations.

System	**Size of box after NPT equilibration run (ÅxÅxÅ; ByteFF-Pol)**	**Density after NPT equilibration (ByteFF-Pol)**	**# of solvent molecules**	**# of salt molecules**
DFETHF	50.00×50.00×50.00	1.29	545	75
TFETHF	49.53×49.53×49.53	1.35	498	75
PFPTHF	49.55×49.55×49.55	1.44	417	75
SFBTHF	49.45×49.45×49.45	1.52	358	75

Reference

(1) Wang, K. H.; Ma, P.; Kim, J.; Han, M.; Amanchukwu, C. V. Monofluorinated Cyclic Ethers Enable Fast Ion Transport in Low-Temperature Lithium Metal Batteries. *ACS Appl Mater Interfaces* **2025**, *17* (24), 35606-35618. DOI: 10.1021/acsami.5c07377.

(2) Plimpton, S. Fast Parallel Algorithms for Short-Range Molecular Dynamics. *Journal of Computational Physics* **1995**, *117* (1), 1-19. DOI: https://doi.org/10.1006/jcph.1995.1039.

(3) Kaminski, G. A.; Friesner, R. A.; Tirado-Rives, J.; Jorgensen, W. L. Evaluation and Reparametrization of the Opls-Aa Force Field for Proteins Via Comparison with Accurate Quantum Chemical Calculations on Peptides. *The Journal of Physical Chemistry B* **2001**, *105* (28), 6474-6487. DOI: 10.1021/jp003919d.

(4) Dodda, L. S.; Cabeza de Vaca, I.; Tirado-Rives, J.; Jorgensen, W. L. Ligpargen Web Server: An Automatic Opls-Aa Parameter Generator for Organic Ligands. *Nucleic Acids Research* **2017**, *45* (W1), W331-W336. DOI: 10.1093/nar/gkx312 (acccessed 12/5/2025).

(5) Storer, J. W.; Giesen, D. J.; Cramer, C. J.; Truhlar, D. G. Class Iv Charge Models: A New Semiempirical Approach in Quantum Chemistry. *Journal of Computer-Aided Molecular Design* **1995**, *9* (1), 87-110. DOI: 10.1007/BF00117280.

(6) Canongia Lopes, J. N.; Pádua, A. A. H.; Shimizu, K. Molecular Force Field for Ionic Liquids Iv: Trialkylimidazolium and Alkoxycarbonyl-Imidazolium Cations; Alkylsulfonate and Alkylsulfate Anions. *The Journal of Physical Chemistry B* **2008**, *112* (16), 5039-5046. DOI: 10.1021/jp800281e.

(7) Martínez, L.; Andrade, R.; Birgin, E. G.; Martínez, J. M. Packmol: A Package for Building Initial Configurations for Molecular Dynamics Simulations. *Journal of Computational Chemistry* **2009**, *30* (13), 2157-2164. DOI: https://doi.org/10.1002/jcc.21224 (acccessed 2026/01/21).

(8) Zheng, T.; Xu, X.; Wang, Z.; Yang, Z.; Wang, Y.; Han, X.; Chen, L.; Mu, Z.; Zhang, Z.; Liu, S.; Gong, S.; Yu, K.; Yan, W. Bridging Quantum Mechanics to Organic Liquid Properties Via a Universal Force Field. 2025; p arXiv:2508.08575.

(9) Abraham, M. J.; Murtola, T.; Schulz, R.; Páll, S.; Smith, J. C.; Hess, B.; Lindahl, E. Gromacs: High Performance Molecular Simulations through Multi-Level Parallelism from Laptops to Supercomputers. *SoftwareX* **2015**, *1-2*, 19-25. DOI: https://doi.org/10.1016/j.softx.2015.06.001.

(10) Eastman, P.; Pande, V. Openmm: A Hardware-Independent Framework for Molecular Simulations. *Computing in Science & Engineering* **2010**, *12* (4), 34-39. DOI: 10.1109/MCSE.2010.27.

(11) Michaud-Agrawal, N.; Denning, E. J.; Woolf, T. B.; Beckstein, O. Mdanalysis: A Toolkit for the Analysis of Molecular Dynamics Simulations. *Journal of Computational Chemistry* **2011**, *32* (10), 2319-2327. DOI: https://doi.org/10.1002/jcc.21787 (acccessed 2025/12/04).

(12) ritesh001. *Byteff2*. GitHub, 2026. https://github.com/ritesh001/byteff2 (accessed.

(13) Meng, E. C.; Goddard, T. D.; Pettersen, E. F.; Couch, G. S.; Pearson, Z. J.; Morris, J. H.; Ferrin, T. A.-O. Ucsf Chimerax: Tools for Structure Building and Analysis. **2023**, (1469-896X (Electronic)).

(14) *Gaussian 16 Rev. C.01*; Wallingford, CT, 2016. (accessed.

(15) Aranda, K.; Manthiram, A. Influence of Anode Reactivity and Chemical Crossover on the Formation of Cathode-Electrolyte Interphase in High-Nickel Layered Oxide Cathodes. *Advanced Energy Materials* **2025**, *15* (47). DOI: 10.1002/aenm.202502617.

(16) Ghanty, C.; Markovsky, B.; Erickson, E. M.; Talianker, M.; Haik, O.; Tal-Yossef, Y.; Mor, A.; Aurbach, D.; Lampert, J.; Volkov, A.; Shin, J. Y.; Garsuch, A.; Chesneau, F. F.; Erk, C. Li+-Ion Extraction/Insertion of Ni-Rich Li1+X(Niycozmnz)Wo2 (0.005<X<0.03; Y:Z=8:1, W≈1) Electrodes: In Situ Xrd and Raman Spectroscopy Study. *ChemElectroChem* **2015**, *2* (10), 1479-1486. DOI: 10.1002/celc.201500160.
(17) Yu, Z.; Rudnicki, P. E.; Zhang, Z.; Huang, Z.; Celik, H.; Oyakhire, S. T.; Chen, Y.; Kong, X.; Kim, S. C.; Xiao, X.; Wang, H.; Zheng, Y.; Kamat, G. A.; Kim, M. S.; Bent, S. F.; Qin, J.; Cui, Y.; Bao, Z. Rational Solvent Molecule Tuning for High-Performance Lithium Metal Battery Electrolytes. *Nature Energy* **2022**, *7* (1), 94-106. DOI: 10.1038/s41560-021-00962-y.
(18) Gallant, B. M.; Hobold, G.; Wang, C.; Steinberg, K.; Li, Y. High Lithium Oxide Prevalence in the Lithium Solid–Electrolyte Interphase for High Coulombic Efficiency. *Nature Energy* **2024**, *9*, 580–591. DOI: 10.21203/rs.3.rs-3203979/v1.
(19) Gong, C.; Pu, S. D.; Gao, X.; Yang, S.; Liu, J.; Ning, Z.; Rees, G. J.; Capone, I.; Pi, L.; Liu, B.; Hartley, G. O.; Fawdon, J.; Luo, J.; Pasta, M.; Grovenor, C. R. M.; Bruce, P. G.; Robertson, A. W. Revealing the Role of Fluoride-Rich Battery Electrode Interphases by Operando Transmission Electron Microscopy. *Advanced Energy Materials* **2021**, *11* (10), 2003118. DOI: 10.1002/aenm.202003118.
(20) Ko, S.; Obukata, T.; Shimada, T.; Takenaka, N.; Nakayama, M.; Yamada, A.; Yamada, Y. Electrode Potential Influences the Reversibility of Lithium-Metal Anodes. *Nature Energy* **2022**, *7* (12), 1217–1224. DOI: 10.1038/s41560-022-01144-0.
(21) Wang, Y.; Chen, W.; Zhao, Q.; Jin, G.; Xue, Z.; Wang, Y.; Mu, T. Ionicity of Deep Eutectic Solvents by Walden Plot and Pulsed Field Gradient Nuclear Magnetic Resonance (Pfg-Nmr). *Phys Chem Chem Phys* **2020**, *22* (44), 25760-25768. DOI: 10.1039/d0cp01431a.
(22) Szczęsna-Chrzan, A.; Vogler, M.; Yan, P.; Żukowska, G. Z.; Wölke, C.; Ostrowska, A.; Szymańska, S.; Marcinek, M.; Winter, M.; Cekic-Laskovic, I.; Wieczorek, W.; Stein, H. S. Ionic Conductivity, Viscosity, and Self-Diffusion Coefficients of Novel Imidazole Salts for Lithium-Ion Battery Electrolytes. *Journal of Materials Chemistry A* **2023**, *11* (25), 13483-13492. DOI: 10.1039/d3ta01217d.